HST Grism Confirmation of Two z ~ 2 Structures from the Clusters around Radio-loud AGN (CARLA) Survey

Gaël Noirot, Joël Vernet, Carlos de Breuck, Dominika Wylezalek, Audrey Galametz, Daniel Stern, Simona Mei, Mark Brodwin, Elizabeth A. Cooke, Anthony H. Gonzalez, et al.

The Astrophysical Journal, 830:90 (26pp), 2016 October 20 doi:10.3847/0004-637X/830/2/90

HST GRISM CONFIRMATION OF TWO $z \sim 2$ STRUCTURES FROM THE CLUSTERS AROUND RADIO-LOUD AGN (CARLA) SURVEY

Gaël Noirot[1,2,3], Joël Vernet[2], Carlos De Breuck[2], Dominika Wylezalek[4], Audrey Galametz[5], Daniel Stern[3], Simona Mei[1,6,7], Mark Brodwin[8], Elizabeth A. Cooke[9], Anthony H. Gonzalez[10], Nina A. Hatch[9], Alessandro Rettura[11], and Spencer Adam Stanford[12]
[1] Université Paris-Diderot Paris VII, Université de Paris Sorbonne Cité (PSC), F-75205 Paris Cedex 13, France; gnoirot@eso.org
[2] European Southern Observatory, Karl-Schwarzschildstrasse 2, D-85748 Garching, Germany
[3] Jet Propulsion Laboratory, California Institute of Technology, 4800 Oak Grove Drive, Pasadena, CA 91109, USA
[4] Johns Hopkins University, Zanvyl Krieger School of Arts & Sciences, 3400 N. Charles Street, Baltimore, MD 21218, USA
[5] Max-Planck-Institut für extraterrestrische Physik, Giessenbachstrasse 1, D-85748 Garching, Germany
[6] GEPI, Observatoire de Paris, PSL Research University, CNRS, University of Paris Diderot, 61, Avenue de l'Observatoire, F-75014 Paris, France
[7] California Institute of Technology, Pasadena, CA 91125, USA
[8] Department of Physics, University of Missouri, 5110 Rockhill Road, Kansas City, MO 64110, USA
[9] School of Physics and Astronomy, University of Nottingham, University Park, Nottingham NG7 2RD, UK
[10] Department of Astronomy, University of Florida, Gainesville, FL 32611-2055, USA
[11] Infrared Processing and Analysis Center, California Institute of Technology, KS 314-6, Pasadena, CA 91125, USA
[12] Department of Physics, University of California, One Shields Avenue, Davis, CA 95616, USA
Received 2016 January 31; revised 2016 July 20; accepted 2016 July 29; published 2016 October 14

ABSTRACT

Using *Hubble Space Telescope* slitless grism data, we report the spectroscopic confirmation of two distant structures at $z \sim 2$ associated with powerful high-redshift radio-loud active galactic nuclei (AGNs). These rich structures, likely (forming) clusters, are among the most distant structures currently known, and were identified on the basis of *Spitzer*/IRAC [3.6]–[4.5] color. We spectroscopically confirm nine members in the field of MRC 2036 −254, comprising eight star-forming galaxies and the targeted radio galaxy. The median redshift is $z = 2.000$. We spectroscopically confirm 10 members in the field of B3 0756+406, comprising 8 star-forming galaxies and 2 AGNs, including the targeted radio-loud quasar. The median redshift is $z = 1.986$. All confirmed members are within 500 kpc (1 arcmin) of the targeted AGNs. We derive median (mean) star-formation rates of $\sim 35\ M_{\odot}\ \mathrm{yr}^{-1}$ ($\sim 50\ M_{\odot}\ \mathrm{yr}^{-1}$) for the confirmed star-forming members of both structures based on their [O III]λ5007 luminosities, and estimate average galaxy stellar masses $\lesssim 1 \times 10^{11}\ M_{\odot}$ based on mid-infrared fluxes and spectral energy distribution modeling. Most of our confirmed members are located above the star-forming main sequence toward starburst galaxies, consistent with clusters at these early epochs being the sites of significant levels of star formation. The structure around MRC 2036−254 shows an overdensity of IRAC-selected candidate galaxy cluster members consistent with being quiescent galaxies, while the structure around B3 0756+406 shows field values, albeit with many lower limits to colors that could allow an overdensity of faint red quiescent galaxies. The structure around MRC 2036−254 shows a red sequence of passive galaxy candidates.

Key words: galaxies: clusters: individual (CARLA J2039-2514, CARLA J0800+4029) – galaxies: high-redshift – galaxies: individual (MRC 2036-254, B3 0756+406)

1. INTRODUCTION

At low to intermediate redshifts ($z \lesssim 1.4$), massive early-type galaxies dominate galaxy cluster cores and form a tight red sequence (e.g., Lidman et al. 2008; Mei et al. 2009). The few studies at higher redshifts suggest that clusters at $z > 1.5$ are still in the process of forming (Snyder et al. 2012; Mei et al. 2015), and that although clusters at these redshifts show a mixed population of both star-forming (SF) and quiescent galaxies, even the reddest (early-type) galaxies show on-going star formation (Mei et al. 2015). Star formation activity has also been observed in the cores of massive galaxy clusters at $z > 1.4$ (e.g., Hayashi et al. 2010; Tran et al. 2010; Zeimann et al. 2013; Alberts et al. 2014; Bayliss et al. 2014). For example, based on a sample of 16 spectroscopically confirmed clusters at $1 < z < 1.5$, Brodwin et al. (2013) showed that at $z > 1.3$ the fraction of SF cluster members increases toward the cluster centers. These results suggest that the majority of star formation actually occurs in high-density environments at early epochs, implying that environmental-dependent quenching has not yet been established at $z > 1.3$. Brodwin et al. (2013) predicted that this transition redshift should be a function of halo mass, with more massive halos transitioning earlier. This is consistent with the findings of Wylezalek et al. (2014) of a $z \sim 3$ transition period for clusters around radio-loud active galactic nuclei (RLAGN), which are extreme objects that tend to reside in the most massive dark matter halos (e.g., Mandelbaum et al. 2009; Hatch et al. 2014; Orsi et al. 2016).

To better understand the dependence of the formation mechanisms of massive galaxies on environment, we must focus on clusters at the relatively unexplored redshift range $z > 1.5$, where major assembly is in progress (e.g., Mancone et al. 2010). Various selection methods are used to find (proto) cluster candidates, e.g., the red sequence (Gladders & Yee 2000; Rykoff et al. 2014; Licitra et al. 2016), a mid-infrared adaptation of the red sequence (Muzzin et al. 2013; Webb et al. 2015), photometric redshifts of infrared-selected samples (Eisenhardt et al. 2008; Stanford et al. 2012; Zeimann et al. 2012), *Spitzer*/IRAC color selection (Papovich 2008; Rettura et al. 2014), overdensities of sub-millimeter sources (Smail et al. 2014; Planck Collaboration XXXIX 2015), X-ray emission (Rosati et al. 1998; Tozzi et al. 2015), and the

Sunyaev Zel'dovich (SZ) effect (Vanderlinde et al. 2010; Bleem et al. 2015). These methods mostly rely on wide-field surveys. Discovering larger samples of galaxy clusters at high redshifts using these techniques therefore requires prohibitive amounts of telescope time over yet wider areas. Moreover, X-ray detections are limited by the surface brightness of the sources[13] dimming as $(1+z)^4$. Both X-ray and SZ selections are also only able to detect very massive structures via their hot intracluster medium, which requires mature, collapsed clusters. Additionally, AGN activity increases for higher redshift clusters (e.g., Galametz et al. 2010; Martini et al. 2013), adding a complication for X-ray and SZ selections. These issues all conspire against finding galaxy clusters at high redshifts, though Mantz et al. (2014) recently reported a massive cluster candidate ($M_{500} \sim (1\text{–}2) \times 10^{14}\ M_{\odot}$) at $z \simeq 1.9$ via a weak X-ray detection, the SZ decrement, and photometric redshifts. Currently, only about 10 galaxy clusters have been spectroscopically confirmed at $z > 1.5$ (e.g., Papovich et al. 2010—independently reported in Tanaka et al. 2010; Stanford et al. 2012; Zeimann et al. 2012; Gobat et al. 2013; Muzzin et al. 2013; Newman et al. 2014; Mei et al. 2015). All of these confirmed clusters are at $z \leqslant 2.0$. A few confirmed clusters and cluster candidates at $1.5 < z < 2$ have significant X-ray detections, implying that they are likely virialized (e.g., Santos et al. 2011; Mantz et al. 2014; Newman et al. 2014). This relatively small number of high-redshift confirmed clusters makes it challenging to draw a clear picture of cluster formation and evolution.

Powerful high-redshift RLAGN are known to preferentially lie in overdense fields (with literature stretching back more than 50 years; e.g., Matthews et al. 1964) and are efficient beacons for identifying large-scale structures and (proto)clusters. Indeed, targeted searches around RLAGN are a proven technique for identifying galaxy clusters at high redshifts (e.g., Stern et al. 2003; Venemans et al. 2007; Galametz et al. 2010; Hatch et al. 2011). Our team has made a major contribution to this effort with a targeted 400 hr *Warm Spitzer Space Telescope* program surveying 420 radio-loud AGNs at $1.3 < z < 3.2$ across the full sky: Clusters Around Radio-Loud AGNs (CARLA, Wylezalek et al. 2013, 2014). Using a simple mid-infrared color-selection technique, we successfully identified nearly 200 promising cluster candidates at $z > 1.3$.

Ground-based observations are challenging for spectroscopically confirming high-redshift galaxy clusters because of atmospheric absorption and emission. In contrast, *Hubble Space Telescope* (*HST*) infrared spectra obtained with the Wide-Field Camera 3 (WFC3) slitless grism are free from atmospheric constraints and are thus ideal for obtaining spectra of high-redshift galaxies, albeit with a low dispersion (46.5 Å/pix^{-1}) and a low resolving power ($R = \lambda/\Delta\lambda = 130$; numbers for G141 grism, Dressel 2014).

Following up on the *Spitzer*/CARLA survey, our team is using the WFC3 slitless G141 grism to study our 20 densest cluster candidates at $1.4 \leqslant z \leqslant 2.8$. This paper presents early results confirming structures around MRC 2036−254 and B3 0756+406, two of the first fields to have their *HST* observations completed. Previous papers from the CARLA project include ground-based spectroscopic confirmation of two (proto)clusters, reported in Galametz et al. (2013) and Rettura et al. (2016, in preparation), ground-based imaging to study the formation histories of CARLA clusters, reported in Cooke et al. (2015, 2016), and a comparison of mass-matched samples of radio-loud and radio-quiet galaxies at $z > 1.3$, showing that RLAGN indeed reside in significantly denser environments (Hatch et al. 2014).

We adopt here the Eisenhardt et al. (2008) criteria of $z > 1$ spectroscopic cluster confirmation: at least five galaxies within a physical radius of 2 Mpc whose spectroscopic redshifts are confined to within $\pm 2000(1 + \langle z_{\rm spec}\rangle)$ km s^{-1}. A significant concern is that this definition alone may also identify groups, protoclusters, sheets, and filaments when applied to grism data. In the lower redshift universe, a more exacting definition for a confirmed galaxy cluster typically also requires: (1) detection of an extended X-ray emitting diffuse intracluster medium, (2) a significant population of early-type (i.e., passive) galaxies, and (3) a centrally concentrated distribution of galaxies. Current literature will often forego the first requirement, particularly for distant clusters, due to the challenges of acquiring such data—and this is particularly problematic for our RLAGN targets due to Inverse Compton scattering of the cosmic microwave background by the hot plasma associated with AGN radio lobes into the X-ray regime. Nonetheless, we show that some CARLA systems have clear overdensities of passive galaxy candidates (see also Cooke et al. 2015; Cooke et al. 2016, in preparation), and Wylezalek et al. (2013) show that the CARLA cluster member candidates are, on average, centrally concentrated around the target RLAGN.

This paper is organized as follows. Section 2 briefly presents the CARLA sample and the overall strategy of our *HST*/CARLA program. Section 3 presents the analysis strategy carried out on the *HST* data, including detection limits. Section 4 presents the results, including cluster membership, star-formation rates (SFRs), and stellar masses. In Section 5, we compare the *HST* results with the CARLA selection method and discuss the results. We summarize our work in Section 6. We also present details on the data analysis in Appendix A. Appendices B and C list the line properties of structure members and non-members, respectively, and we present notes on individual sources in Appendix D. Throughout, all magnitudes are expressed in the AB photometric system, and we use a flat ΛCDM cosmology with $H_0 = 70$ km Mpc^{-1} s^{-1}, $\Omega_\Lambda = 0.7$, and $\Omega_m = 0.3$.

2. OBSERVATIONS

2.1. The CARLA Sample

The CARLA sample consists of *Spitzer*/IRAC channels 1 and 2 (3.6 and 4.5 μm bands, respectively) observations of 420 fields around powerful RLAGN obtained during a 400 hr *Warm Spitzer* Cycle 7 and 8 snapshot program. Each image covers an area of 5.2×5.2 arcmin^2 with an original sampling of 1.22 arcsec pix^{-1} reprocessed to 0.61 arcsec pix^{-1}. The data reach 95% completeness at 22.8 mag and 22.9 mag for the 3.6 μm and 4.5 μm bands, respectively. The program imaged the fields of 209 high-redshift radio galaxies (HzRGs) and 211 radio-loud quasars (RLQs), uniformly selected in radio-luminosity over the redshift range $1.3 < z < 3.2$ (with rest-frame $L_{500\,\rm MHz} \geqslant 10^{27.5}$ W Hz^{-1}). The HzRGs (type-2 RLAGN) were selected from the updated compendium of Miley & De Breuck (2008), and the RLQs (type-1 RLAGN) were selected from the Sloan Digital Sky Survey (SDSS,

[13] With the caveat that, based on the low-redshift Vikhlinin et al. (2009) scaling relations, Churazov et al. (2015) showed that at higher redshifts ($z \simeq 1$–2), clusters as massive as $z \sim 0$ clusters should be as easily detectable.

Schneider et al. 2010) and 2dF QSO Redshift Survey (2QZ, Croom et al. 2004). Galaxy cluster candidates were then identified as IRAC color-selected galaxy overdensities in the fields of the targeted RLAGN. We applied the color cut $([3.6]-[4.5])_{AB} > -0.1$ mag, which reliably identifies $z > 1.3$ sources (Papovich 2008). Galaxy cluster candidates are defined as fields showing a $>2\sigma$ overdensity of IRAC color-selected sources compared to the blank field surface density of similarly selected sources, as measured in the *Spitzer* UKIDSS Ultra-Deep Survey (SpUDS; P.I. Dunlop). We measured the density of IRAC color-selected sources within $1'$ radius apertures centered on the RLAGN (~500 kpc at $z \sim 2$). We identified 178 cluster candidates among the 420 fields. The galaxy density of these cluster candidates strongly peaks toward the position of the targeted RLAGN, suggesting that the clusters are reliable and that the RLAGN reside at the cluster cores. Detailed descriptions of the sample and initial scientific results are presented in Wylezalek et al. (2013, 2014).

2.2. The CARLA HST Program

Among the 178 CARLA cluster candidates, we selected the 20 richest fields as the most promising targets for additional study. These fields are 5.8σ–9.0σ overdense above the mean SpUDS density and the associated RLAGN at the center of each field cover the redshift range of $1.4 < z < 2.8$. Ten of the twenty fields are associated with HzRGs and the other ten are associated with RLQs. Our team was awarded 40 *HST* orbits in a Cycle 22 WFC3 program to image and obtain spectroscopy of these 20 CARLA fields with the primary goal of spectroscopically confirming the cluster candidates (Program ID: 13740). Each field is visited twice using different orientations to mitigate contamination from overlapping spectra. The first field was observed in 2014 October and the whole program was completed in 2016 April. For each visit, our program obtains 0.5 ks *F*140*W* direct imaging and 2 ks G141 slitless grism spectroscopy.

Each image covers a field of view of 2×2.3 arcmin^2 at a sampling of 0.13 arcsec pix^{-1}. The G141 grism covers the wavelength range of $\lambda = (1.08$–$1.70)$ μm with a throughput >10% and was chosen because it samples Hα at $0.65 < z < 1.59$, [O III] at $1.16 < z < 2.40$, Hβ at $1.22 < z < 2.50$, and [O II] at $1.90 < z < 3.56$, enabling us to identify strong galaxy features at the redshifts of our cluster candidates ($1.4 < z < 2.8$) and potentially measure dust extinction via the Balmer decrement for $1.22 < z < 1.59$.

2.3. Spectroscopy

2.3.1. HST Observations of CARLA J2039−2514 and CARLA J0800+4029

The field around MRC 2036−254 (HzRG at $z = 1.997$) and the field around B3 0756+406[14] (RLQ at $z = 2.004$) were observed in 2014 October and November, respectively, partitioned in two single-orbit visits each, using two different orientations. Total exposure times on the field around MRC 2036−254 (B3 0756+406) reached 4023 s (4123 s) in grism mode and 1023 s (1073 s) in direct imaging mode. Table 1 lists the observation dates, exposure times, and orientation angles. We refer to the spectroscopically confirmed structures by their CARLA names, CARLA J2039−2514 and CARLA J0800+4029.

Each visit was divided into four dithered blocks of exposures, with the direct images taken just after the grism exposures to enable wavelength calibration of the spectra based on source position. We retrieved calibrated and flat-fielded individual exposures (FLT)[15] from MAST,[16] which uses the most up-to-date calibration files for WFC3. These were our primary data products before further reduction and extraction of the spectra.

2.3.2. B3 0756+406 Palomar Spectrum

Because the very broad lines of B3 0756+406 in our *HST* spectroscopy prevent us from measuring a reliable redshift (see Appendix D), and because of the relatively low signal-to-noise ratio of its SDSS spectrum, we obtained an optical spectrum of the source on UT 2015 February 17 using the Double Spectrograph on the Hale 200″ telescope at Palomar Observatory. The conditions were relatively clear, but not photometric, with ~1.″3 seeing. We observed the target through a 1.″5 slit for two 900 s exposures using the 600 ℓmm^{-1} grating on the blue arm of the spectrograph ($\lambda_{blaze} = 4000$ Å), the 316 ℓmm^{-1} grating on the red arm of the spectrograph ($\lambda_{blaze} = 7500$ Å), and the 5500 Å dichroic. The data were processed using standard techniques within IRAF, and flux calibrated using standard stars from Massey & Gronwall (1990) observed on the same night. The optical spectrum (Figure 1) shows strong and broad emission lines from Lyα, C IV, C III, and Mg II at a redshift $z = 2.004 \pm 0.002$, slightly lower than the redshift $z = 2.021$ derived from the lower-quality SDSS spectrum. Narrow self-absorption is seen in all but the C III line.

3. DATA PROCESSING

3.1. Data Reduction

Our grism data contain traces of several hundred objects (see Figure 2), including first and zeroth orders and even additional orders (−1, +2) in the case of bright objects. Therefore, in addition to standard reduction procedures (cosmic-ray rejection, sky subtraction, etc.) spectra need to be carefully extracted. We generally follow the steps presented in the WFC3 IR grism cookbook[17] (v1.3), applying identical methods for both fields.

We combine the individual *F*140*W* exposures using the aXe software (v2.2.4) to create deep drizzled direct images of the fields. From these images, we perform source extraction using SExtractor (Bertin & Arnouts 1996). In this step, we create two catalogs: a deep catalog cleaned by hand from spurious detections (the master catalog), and a shallow catalog with a more conservative magnitude limit. The latter allows us to subtract the sky background from the grism images in a later step.[18] Since our targets were selected as CARLA overdense fields, we cross-correlate the color-selected IRAC $z > 1.3$ candidates with our *HST* master catalog, even though, in practice, we extract and analyze all *HST* sources (see details in Appendix A.3).

[14] Note that Wylezalek et al. (2013, 2014) refer to this source by its SDSS coordinates, SDSS J080016.09+402955.6, rather than by its B3 radio catalog name.

[15] See details in Appendix A.1.

[16] Mikulski Archive for Space Telescope: https://archive.stsci.edu.

[17] Available at http://axe-info.stsci.edu.

[18] See additional details of these steps in Appendix A.2.

Table 1
HST WFC3 Observations

Target	UT Date	Position Angle[a] (degree)	*F*140*W*/G141 Exp. Time (s)
MRC 2036−254	2014 Oct 14	−62	512/2012
	2014 Oct 15	−39	512/2012
B3 0756+406	2014 Nov 03	+125	537/2062
	2014 Nov 07	+162	537/2062

Note.
[a] East of north.

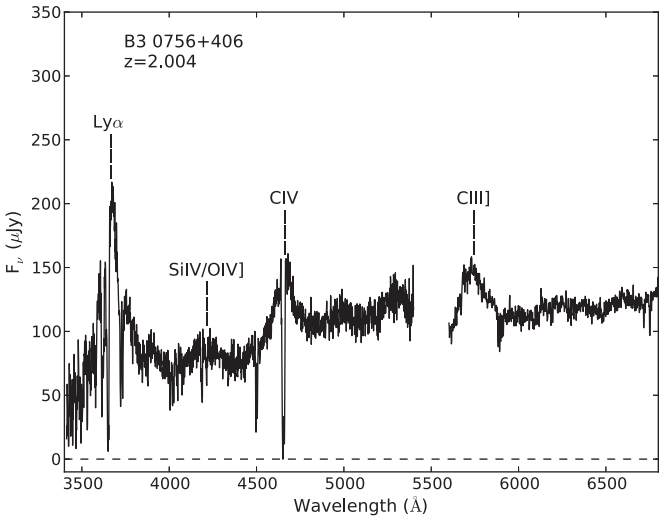

Figure 1. Optical Palomar spectrum of B3 0756+406, the targeted RLQ of CARLA J0800+4029. We identify Lyα, C IV, C III, and Mg II (λ_{obs} = 8411 Å, not shown), and measure a new redshift of $z = 2.004 \pm 0.002$.

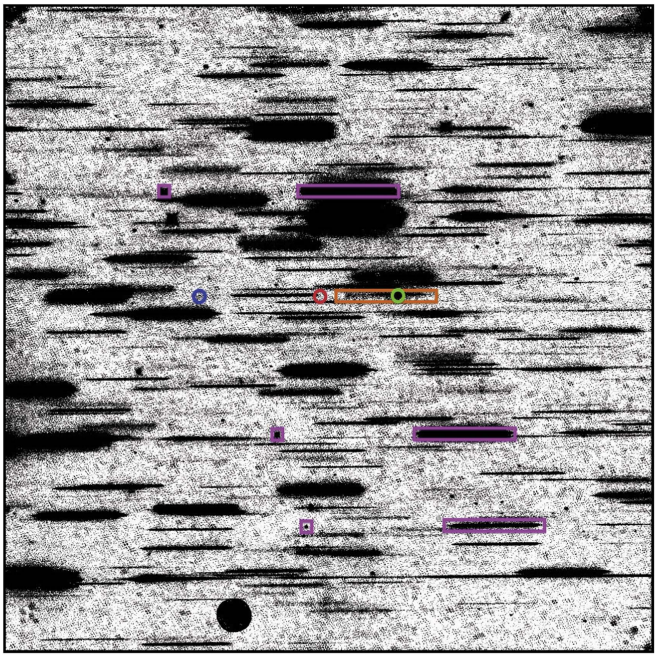

Figure 2. Combined G141 grism exposures of the first visit to MRC 2036 −254. The red circle shows the physical location of the HzRG. Its zeroth order is shown by the blue circle, and the trace of its first order by the orange rectangle. The green circle on top of the rectangle shows the location of the bright [O III] emission line of the source. The other purple squares and rectangles highlight some zeroth and first orders of bright sources in the field.

The master catalog is then projected back onto each individual direct exposure and the background level is subtracted from each grism exposure using up-to-date master sky background (v1.0) and grism mode configuration files (v2.5).[19] Details of these two steps are presented in Appendix A.4.

3.2. Extraction of Spectra and Contamination Models

We then extract individual spectra from each scaled grism frame based on source positions and sizes stored in the individual master catalogs, and stack the spectra of the same observation/orientation. The aXe task `axecore` determines contamination estimates from neighboring and/or overlapping objects. We use the "Gaussian" method of the qualitative contamination model as a first approximation, adopting a width scale factor of one instead of the standard factor of three, which we found makes the spectral traces in the spatial (cross-dispersion) direction too wide.[20] To obtain deep 2D first order spectra of constant dispersion in wavelength and linear spatial sampling, we run the tasks `drzprep` and `axedrizzle`. Note that we keep each orientation separate in order to better handle contamination issues. We obtain for each available orientation a deep 2D cutout of the first spectral order of each source as well as a deep 2D cutout containing the traces of its possible contaminants estimated from the "Gaussian" contamination model.

Finally, we manipulate the 2D cutouts to extract our own 1D spectra, flux calibrated using the G141 first order sensitivity function. The software identifies continuum and zeroth orders of possible contaminants on the 2D cutouts.

3.3. Detection Limits and Noise Level

3.3.1. Imaging Noise Level

We measure the *F*140*W* noise level from object-free regions based on the SExtractor segmentation map corresponding to our deep catalog. We use this map to mask all detected sources, and we measure the noise level by randomly placing 5000 non-overlapping 0.″4 diameter apertures[21] on the unmasked area covered by both orientations. For both fields, the noise values follow a Gaussian distribution with best-fit values given in Table 2. The images of both fields have 1σ noise levels of $\sim 2.5 \times 10^{-21}$ erg s^{-1} cm^{-2} Å^{-1}, corresponding to ∼26.6 mag (AB) at 5σ.

[19] Available at http://www.stsci.edu/hst/wfc3/analysis/grism_obs/calibrations/wfc3_g141.html.
[20] See more details on the contamination models in Appendix A.5.
[21] Typical size of our *HST* sources.

Table 2
Noise Levels

Target	F140W		G141
	σ[a]	mag$_{AB}$ (5σ)	σ[b]
MRC 2036−254	2.7	26.5	⋯
Orient01	⋯	⋯	51
Orient02	⋯	⋯	60
B3 0756+406	2.4	26.7	⋯
Orient01	⋯	⋯	44
Orient02	⋯	⋯	59

Notes.
[a] Standard deviation in flux density (10^{-21} erg s^{-1} cm^{-2} Å^{-1}).
[b] Same as [a] but at 15000 Å.

3.3.2. Spectroscopic Noise Level

We use the full contamination image produced by aXe as a mask on the G141 frames to compute the G141 noise distribution over spectrum-free regions. Because aXe does not produce a co-added image for the G141 exposures, we use the IRAF task `imcombine` on the G141 sky-subtracted frames and corresponding contamination model frames to produce the grism combined (averaged) images of both the contamination model and the real exposures. For both fields, the noise distribution closely follows a Gaussian distribution. For the spectroscopic analysis, we calibrate this baseline pixel noise level to the relevant wavelength under consideration using the G141 sensitivity function, and this provides the internal uncertainty for flux measurements. Table 2 provides the values at 15000 Å, of the order of 5×10^{-20} erg s^{-1} cm^{-2} Å^{-1}. The contamination model contours shown on the spectral 2D cutouts (see Appendix D) represent 1σ, 2σ, 5σ, and 10σ deviations above the mean level.

3.3.3. Line Detection Limit

The grism sensitivity is maximal and roughly constant over the wavelength range of (14500–15500) Å, where Hβ and [O III] fall at $z \sim 2$. We use cluster member spectra of undetected Hβ emission lines to determine our detection limit (note that all cluster members have detected [O III] lines). We generate 100 Gaussians of evenly spaced height values in the range of (0–3) $\times$ 10^{-19} erg s^{-1} cm^{-2} Å^{-1} that we add to the spectra at the expected locations of Hβ. Using the same fitting procedure as described in Section 3.4.1, we define our detection limit as the minimum flux, which has a signal-to-noise ratio $\geqslant$5 and a measured-to-true flux ratio in the range of 0.8–1.2. Our detection limit differs slightly from spectrum to spectrum, but is generally in the range of (1.2–4.0) $\times$ 10^{-17} erg s^{-1} cm^{-2}. We adopt the mean value, 2.5×10^{-17} erg s^{-1} cm^{-2}, as our detection limit for both fields.

3.4. Measurements

3.4.1. Emission Line Fitting

We determine the redshift of the sources and emission line fluxes using the python version of `mpfit`[22], a Levenberg–Marquardt least-squares minimization fitting procedure. When required (e.g., for all cluster members), we fit the [O III] doublet (λ4959, λ5007) with two Gaussians constrained to have the same width, same redshift, and a 1:3.2 flux ratio (Osterbrock 1989). Simultaneously, we fit the continuum using a third order polynomial and include a third Gaussian corresponding to Hβ, constrained to have the same redshift as [O III]. We substitute [O III] with, or add to the model, other Gaussians to account for Hα or [O II] when required (e.g., for non-cluster members). Table 3 shows the redshifts and emission line fluxes of our cluster members, and Table 4 presents the redshifts of non-cluster members.

3.4.2. Uncertainties

From the WFC3 Data Handbook, the internal accuracy of the G141 grism dispersion is 0.25 pixel for G141. In addition, the wavelength calibration of the spectroscopy depends on the accuracy of the object centroid in the direct image, and the accuracy of the grism wavelength zero point based on the direct image source positions. Small offsets between the orientations will also produce spectral offsets. The handbook recommends a calibration uncertainty of 0.3 pixel, corresponding to a wavelength uncertainty of 20 Å or a redshift uncertainty of 0.003–0.006 at $z = 2$, depending on the identified spectral feature. The internal error on the emission line fluxes is simply the 1σ level of the grism detector noise distribution (see Section 3.3.2).

The fitting procedure described in Section 3.4.1 produces a formal 1σ error on all measured parameters, directly given by `mpfit`. To obtain the global parameter uncertainties (i.e., the measurement errors from the fitting procedure), we scale the formal errors with the reduced χ^2 of the fit (χ^2 divided by the number of degrees of freedom): scaled_error = formal_error $\times$ $\sqrt{\chi^2/\mathrm{dof}}$. The total redshift uncertainty is the quadratic sum of the internal and measurement errors. However, since we use the flux internal error as an additional input parameter to the fitting procedure, we only use `mpfit` scaled errors to calculate the total flux uncertainties (i.e., the scaled errors already take the flux internal error into account).

4. RESULTS

We visually inspect all extracted spectra, and use our fitting procedure on those showing clear emission lines. The 2D cutouts, 1D spectra, and contamination contours of all cluster members are shown in Appendix D, including their direct image stamps.

4.1. Redshift Determination

We have three proxies for identifying cluster members: emission lines, IRAC [3.6]–[4.5] colors, and the redshift priors of the targeted RLAGN. We assign three different quality redshifts; A, B$^+$, and B$^-$, defined as follows.

1. *Quality A*. When several lines are identified, we assign a quality A to the source redshift, and the redshift is considered to be very secure.
2. *Quality B$^+$*. When only one line is detected but the source has a robust IRAC counterpart, we use the mid-infrared color to determine the most likely line identification (e.g., [O II], [O III], or Hα) and assign a quality B$^+$ to the redshift. Such sources are considered to have relatively secure redshifts.

[22] Available here: http://code.google.com/p/agpy/source/browse/trunk/mpfit/mpfit.py?r=399.

Table 3
Confirmed Cluster Members

Field	Object	R.A. (hh:mm:ss.ss)	Decl. (dd:mm:ss.s)	$F140W$ (AB)	[3.6] (AB)	[4.5] (AB)	$f_{[\mathrm{O\ III}]}$[a]	$f_{\mathrm{H}\beta}$[a]	z	Quality[b]	Remarks[c]
CARLA J2039−2514	119	20:39:28.51	−25:14:31.2	22.35 ± 0.02	20.87 ± 0.02	20.88 ± 0.02	6.5 ± 2.9	⋯	1.987 ± 0.007	B^+	SF
	174	20:39:22.61	−25:14:16.0	22.87 ± 0.03	22.09 ± 0.06	22.13 ± 0.05	5.1 ± 1.5	⋯	2.000 ± 0.007	B^+	SF
	281	20:39:22.14	−25:15:08.6	23.98 ± 0.06	⋯	⋯	8.4 ± 3.2	⋯	2.002 ± 0.008	B^-	SF
	306	20:39:24.49	−25:14:30.7	20.94 ± 0.01	19.99 ± 0.01	19.79 ± 0.01	74.7 ± 3.8	7.3 ± 3.1	1.997 ± 0.004	A	HzRG
	306b[d]	20:39:24.52	−25:14:30.6	⋯	⋯	⋯	59.5 ± 2.7	17.7 ± 4.0	1.999 ± 0.004	A	AGN
	356	20:39:24.61	−25:14:34.2	24.41 ± 0.07	⋯	⋯	8.0 ± 1.9	⋯	1.999 ± 0.005	B^-	SF
	360	20:39:25.74	−25:14:07.9	23.92 ± 0.06	⋯	⋯	10.1 ± 2.8	⋯	2.006 ± 0.004	B^-	SF
	697	20:39:21.32	−25:13:55.6	23.80 ± 0.05	⋯	⋯	5.1 ± 1.8	⋯	2.001 ± 0.006	B^-	SF
	44300	20:39:24.57	−25:14:22.2	25.66 ± 0.16	⋯	⋯	3.5 ± 1.3	⋯	2.002 ± 0.005	B^-	SF
	90000	20:39:21.33	−25:14:25.3	26.35 ± 0.24	⋯	⋯	4.0 ± 1.5	⋯	1.995 ± 0.005	B^-	SF
CARLA J0800+4029	146	08:00:12.40	+40:30:40.4	24.89 ± 0.09	⋯	⋯	4.4 ± 1.8	⋯	1.998 ± 0.007	B^-	SF
	371	08:00:16.11	+40:29:55.6	19.66 ± 0.01	17.64 ± 0.01	17.22 ± 0.01	⋯	⋯	2.004 ± 0.002[e]	A	QSO
	372	08:00:15.94	+40:29:53.2	20.96 ± 0.01	Blend	Blend	22.8 ± 1.7	⋯	2.001 ± 0.004	A	SF
	401	08:00:18.54	+40:30:39.0	25.94 ± 0.24	⋯	⋯	5.4 ± 3.4	⋯	1.980 ± 0.009	B^-	SF
	436	08:00:14.76	+40:29:48.1	22.05 ± 0.01	20.33 ± 0.01	20.19 ± 0.01	5.6 ± 2.1	⋯	1.969 ± 0.007	B^+	SF
	443	08:00:17.29	+40:30:30.0	24.52 ± 0.07	⋯	⋯	7.6 ± 1.3	⋯	1.992 ± 0.004	B^-	SF
	542	08:00:11.95	+40:29:24.3	22.12 ± 0.01	20.83 ± 0.02	20.78 ± 0.02	18.4 ± 5.1	⋯	1.964 ± 0.007	B^+	SF
	591	08:00:11.61	+40:29:38.0	25.82 ± 0.18	⋯	⋯	3.4 ± 1.6	⋯	1.975 ± 0.007	B^-	SF
	749	08:00:16.12	+40:28:57.3	22.00 ± 0.02	20.30 ± 0.01	20.10 ± 0.01	27.1 ± 2.2	27.8 ± 3.5	2.001 ± 0.004	A	QSO
	767	08:00:18.96	+40:29:38.9	23.81 ± 0.05	23.84 ± 0.24	22.97 ± 0.09	4.2 ± 1.2	⋯	1.978 ± 0.004	B^+	SF

Notes.
[a] Flux in units of 10^{-17} erg s^{-1} cm^{-2}.
[b] See Section 4.1.
[c] SF: star-forming galaxy, HzRG: high-redshift radio galaxy, AGN: active galactic nucleus, QSO: quasi-stellar object.
[d] This source is the companion to MRC 2036−254 (#306).
[e] Determined from the Palomar spectrum described in Section 2.3.2.

Table 4
Confirmed Non-cluster Members

Field	Object	R.A. (hh:mm:ss.ss)	Decl. (dd:mm:ss.s)	$F140W$ (AB)	z	Quality[a]	Line(s) fitted[b]
CARLA J2039−2514	54	20:39:28.65	−25:14:51.9	21.79 ± 0.01	1.219 ± 0.005	A	Hα
	83	20:39:28.83	−25:14:36.9	21.72 ± 0.01	0.984 ± 0.005	B^+	Hα
	133	20:39:21.92	−25:14:19.3	24.42 ± 0.08	2.289 ± 0.006	A	[O III], [O II]
	261	20:39:25.48	−25:13:35.9	24.34 ± 0.06	1.379 ± 0.004	A	[O III], Hα
	265	20:39:25.05	−25:13:49.7	21.16 ± 0.01	0.813 ± 0.003	B^-	Hα
	298	20:39:24.13	−25:14:24.5	22.68 ± 0.02	0.944 ± 0.004	B^+	Hα
	382	20:39:25.40	−25:14:25.3	24.01 ± 0.09	1.452 ± 0.006	A	[O III], Hα
	422	20:39:26.81	−25:14:06.4	22.71 ± 0.02	2.130 ± 0.004	A	[O III], [O II]
	429	20:39:25.05	−25:14:55.5	21.86 ± 0.02	1.908 ± 0.008	B^+	[O III]
	496	20:39:24.63	−25:15:29.5	25.62 ± 0.17	1.934 ± 0.006	B^-	[O III]
	564	20:39:28.53	−25:14:13.6	19.62 ± 0.01	0.714 ± 0.004	A	Hα
	564b[c]	20:39:28.53	−25:14:13.6	⋯	0.7	A	Hα (visual)
	565	20:39:28.52	−25:14:15.3	20.98 ± 0.01	0.709 ± 0.005	A	Hα
	570	20:39:26.13	−25:15:17.6	23.70 ± 0.05	1.330 ± 0.006	A	[O III], Hα
	579	20:39:27.13	−25:14:57.8	23.70 ± 0.05	1.444 ± 0.004	A	[O III], Hα
	581	20:39:25.77	−25:15:33.6	23.19 ± 0.03	1.381 ± 0.006	A	[O III], Hα
	582	20:39:27.74	−25:14:42.8	24.52 ± 0.06	1.360 ± 0.004	A	[O III], Hα
	588	20:39:27.93	−25:14:40.1	22.10 ± 0.02	1.472 ± 0.006	A	[O III], Hα
	619	20:39:20.18	−25:14:56.0	22.91 ± 0.03	1.216 ± 0.004	B^+	Hα
	639	20:39:21.03	−25:14:18.1	22.39 ± 0.02	1.171 ± 0.004	A	Hα
	667	20:39:20.73	−25:14:19.5	21.57 ± 0.01	1.151 ± 0.003	B^-	Hα
	20700	20:39:29.21	−25:14:18.0	25.45 ± 0.15	1.732 ± 0.007	B^-	[O III]
	55200	20:39:26.54	−25:14:04.2	25.64 ± 0.13	2.094 ± 0.004	B^-	[O III]
CARLA J0800+4029	166	08:00:13.74	+40:30:53.6	23.88 ± 0.05	2.345 ± 0.005	A	[O III], [O II]
	198	08:00:14.20	+40:30:49.9	22.72 ± 0.02	1.927 ± 0.007	B^-	[O III]
	204	08:00:10.62	+40:29:47.4	22.55 ± 0.02	1.745 ± 0.006	B^+	[O III]
	294	08:00:18.39	+40:29:49.7	22.16 ± 0.01	0.753 ± 0.005	B^-	Hα
	313	08:00:17.38	+40:29:59.1	22.70 ± 0.02	2.171 ± 0.005	B^-	[O III]
	349	08:00:12.42	+40:28:46.5	22.54 ± 0.02	2.234 ± 0.005	B^-	[O III]
	355	08:00:13.63	+40:29:10.0	22.76 ± 0.02	1.916 ± 0.009	B^+	[O III]
	357	08:00:18.59	+40:30:31.3	22.44 ± 0.02	1.905 ± 0.005	B^+	[O III]
	387	08:00:14.23	+40:29:26.4	21.50 ± 0.01	1.923 ± 0.005	B^+	[O III]
	554	08:00:13.72	+40:30:01.4	23.96 ± 0.07	1.876 ± 0.006	B^-	[O III]
	584	08:00:15.62	+40:29:14.6	22.84 ± 0.02	0.799 ± 0.003	B^+	Hα
	587	08:00:16.78	+40:31:01.1	22.08 ± 0.01	1.258 ± 0.003	A	Hα
	673	08:00:16.41	+40:29:22.2	22.65 ± 0.02	1.743 ± 0.007	B^+	[O III]
	697	08:00:19.04	+40:29:57.6	23.50 ± 0.04	2.092 ± 0.004	B^+	[O III]
	746	08:00:19.47	+40:29:51.2	23.01 ± 0.03	1.873 ± 0.006	B^+	[O III]
	776	08:00:19.20	+40:29:27.4	23.86 ± 0.06	1.439 ± 0.007	A	[O III], Hα

Notes.
[a] See Section 4.1.
[b] Note that, in some cases, additional lines have been identified but not fitted.
[c] This source is a second component to #564, blended in the $F140W$ imaging.

3. *Quality B^-*. When only one line is robustly detected but the source does not have an IRAC counterpart, the line identification is less secure and we assign a quality B^- to the redshift. Such redshifts are considered likely correct, albeit with the potential for some mis-identifications.

When only one line is detected, we assume that it is a strong line characteristic of star formation or AGN activity, given our observation depth. We discard the possibility of recovering a Lyα line because it would imply a redshift >8, and therefore we only consider [O II]λ3727, [O III]$\lambda\lambda$4959, 5007, and Hα. We also use [O III] or Hα non-detections to disentangle line identifications assuming a [O III]:Hα ratio of unity; empirically, the line ratio has a dispersion of a factor of approximately two (e.g., Mehta et al. 2015). We do not use [O II] non-detections because the line can be below our detection limit when the typically stronger [O III] line is detected. In cases where a source is detected in our *Spitzer* data, we use its IRAC mid-infrared color to segregate $z > 1.3$ galaxies from foreground sources since, empirically, galaxies at $z > 1.3$ tend to have $([3.6]-[4.5])_{AB} > -0.1$ mag (Papovich 2008; see Galametz et al. (2012) for a comprehensive discussion of possible contaminants). Based on the 11 quality A redshifts from our spectroscopic sample with *Spitzer* detections, we find that eight out of nine sources with $([3.6]-[4.5])_{AB} > -0.1$ mag are at $z > 1.3$, while one out of two sources with bluer mid-infrared colors is at $z < 1.3$. This is consistent with Papovich (2008), who found that red mid-infrared colors effectively identify distant ($z > 1.3$) galaxies, but that distant galaxies do not exclusively have red mid-infrared colors. Cluster member sources are identified based on the [O III] line, which is observed at ∼15000 Å at $z \sim 2$, the redshift of the targeted RLAGN. Based on our identification scheme, a single emission line observed around 15000 Å can also correspond to [O II] at

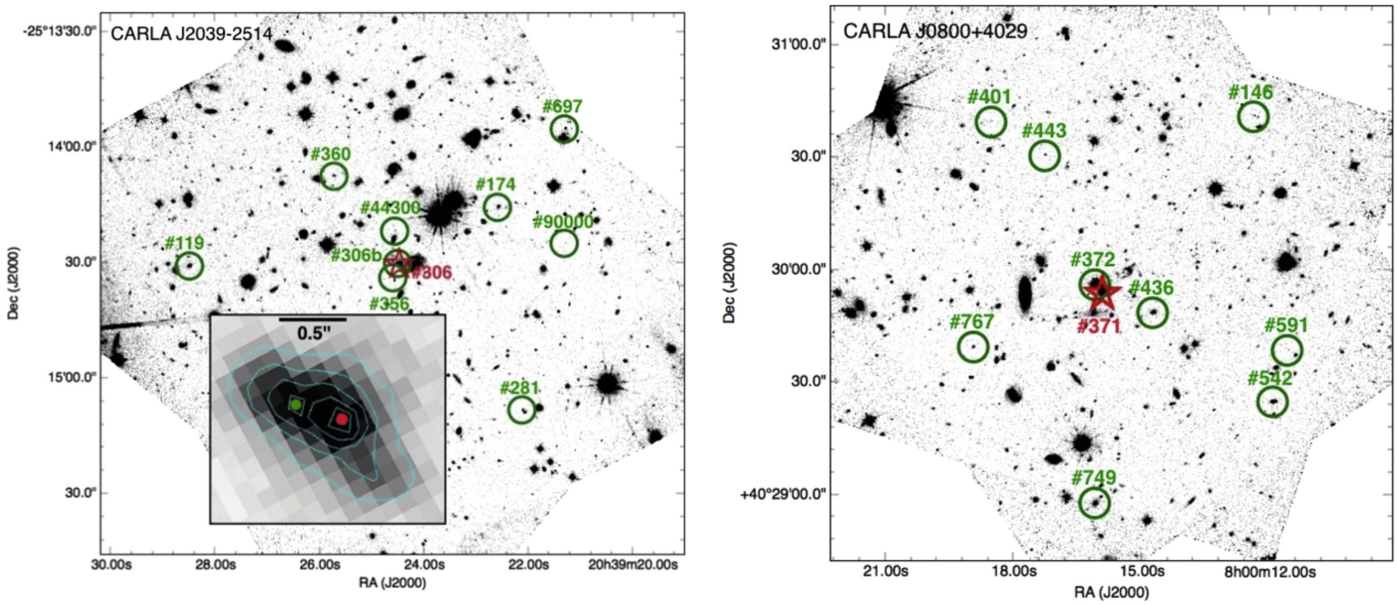

Figure 3. *F*140*W* images of our two RLAGN fields, showing the spatial distribution of CARLA J2039−2514 (left) and CARLA J0800+4029 (right) confirmed members. North is up and east is to the left. The red stars indicate the RLAGN, and the green circles indicate confirmed member galaxies. The inset in the left panel shows a close-up of the targeted HzRG, MRC 2036−254 (#306). The red dot shows the position of the source, and the green dot shows the position of its companion #306 b; these two components are highlighted by contour lines.

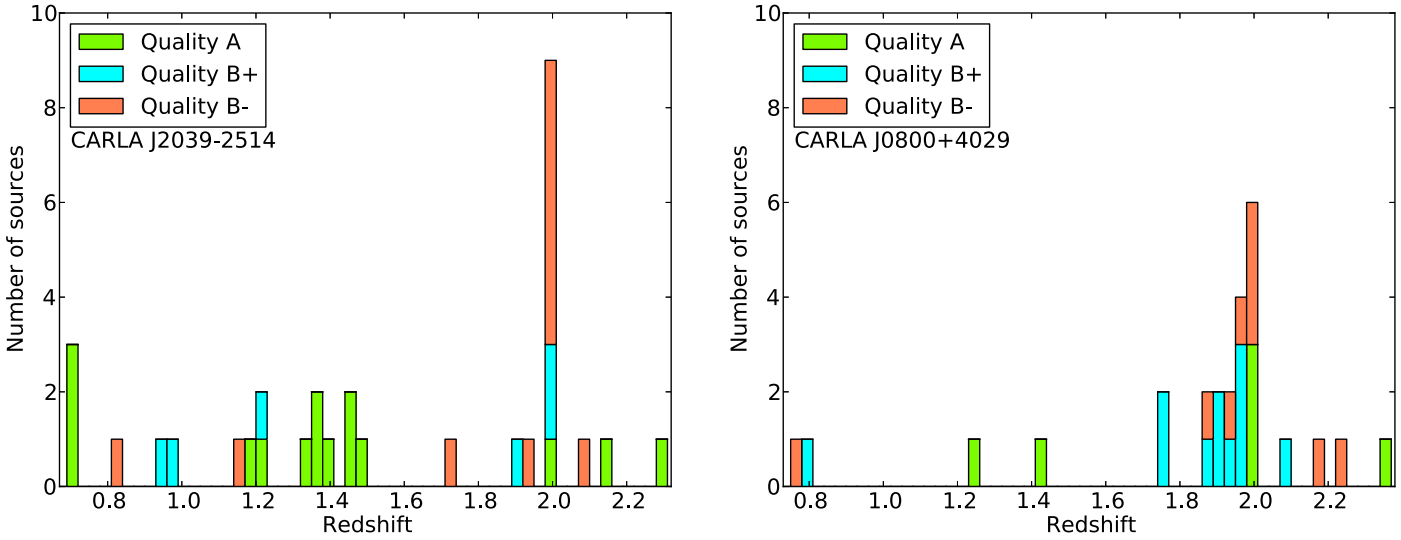

Figure 4. Distribution of WFC3 grism redshifts in the fields around MRC 2036−254 (left) and B3 0756+406 (right). The bin size is 0.03 in redshift. The quality flags are described in Section 4.1. Both fields have strong peaks at $z \simeq 2$, with a larger scatter for the latter field. Cluster member redshifts are listed in Table 3, and redshifts of other sources are listed in Table 4.

$z \sim 3$. However, based on the 79,609 *HST* grism redshifts from the 3D-*HST* field survey (Momcheva et al. 2015), there are 405 [O III] and 63 [O II] emitters above our detection limit in the wavelength range of (14840–15042) Å. With eight (CARLA J2039−2514) and seven (CARLA J0800+4029) quality B members (see Section 4.2 and Figure 5), we therefore expect that no more than one spectroscopically confirmed source per structure is likely [O II] at $z \sim 3$ rather than [O III] at the redshift of the RLAGN. We performed two independent redshift determinations (GN and DS), which yield consistent assessments. Table 3 shows the cluster member properties, and Figure 3 shows their spatial distributions. Table 4 lists the measured redshifts of other sources in the *HST* fields of view, Figure 4 shows the redshift distribution of identified sources in each field, and Figure 5 highlights the cluster redshift distributions. We measure our member properties independently for both orientations when possible, and determine the final physical parameters as the average of the results from the two orientations, with uncertainties added in quadrature.

4.2. Cluster Membership

Eisenhardt et al. (2008) defined a spectroscopically confirmed $z > 1$ cluster as a structure containing at least five galaxies within a physical radius of 2 Mpc whose spectroscopic redshifts are confined to within $\pm 2000(1 + \langle z_{\rm spec} \rangle)$ km s^{-1}. From emission lines and IRAC colors (when available), we identify nine members in CARLA J2039−2514 at $\langle z \rangle = 1.999 \pm 0.002$ (median 2.000). This includes the

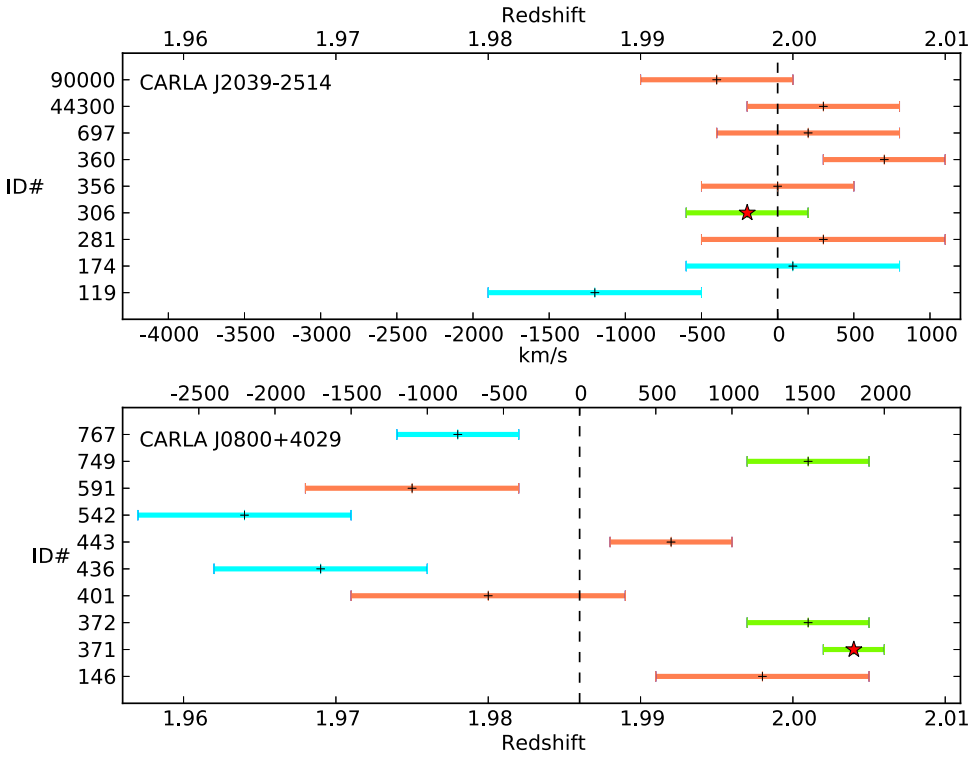

Figure 5. Redshift distribution of the members of CARLA J2039−2514 (top) and CARLA J0800+4029 (bottom). The panels show the redshift of each source and its uncertainty. The vertical dashed lines indicate the mean redshift of each cluster. Both panels show the same redshift range (i.e., $1.956 < z < 2.011$). The velocity shifts relative to each cluster mean redshift are also indicated on the horizontal axes. Line colors correspond to the redshift qualities of Figure 4, and the red stars indicate the targeted RLAGN. The redshift distribution of CARLA J2039−2514 members spans 0.03 in redshift, whereas the one of CARLA J0800+4029 members spans 0.05 in redshift, including 1σ uncertainties.

RLAGN, which is kinematically complex, showing two components, potentially a dual AGN, separated by 0.″5 (see Figure 3 inset). The standard deviation between the members is 0.005 in redshift. We identify 10 members in CARLA J0800 +4029 at $\langle z \rangle = 1.986 \pm 0.002$ (median 1.986), with a 0.014 deviation between the members. In both cases, all confirmed members are located within 1′ radii, corresponding to projected radii of 500 kpc at the redshifts of the RLAGN (1.5 Mpc co-moving). As seen in Figure 5, members are confined within $[-1200; +700]$ km s^{-1} of their cluster mean redshift for CARLA J2039−2514, spanning 0.02 in redshift space (removing one outlier, we have $[-500; +600]$ km s^{-1} for eight of the nine confirmed members), and within $[-2300; +1700]$ km s^{-1} for CARLA J0800+4029, spanning 0.04 in redshift space.

While these two structures conform to the Eisenhardt et al. (2008) confirmation criteria, these criteria were initially developed for ground-based spectroscopic programs, and have the potential to misidentify clusters less massive structures such as protoclusters, groups, sheets, and filaments. While keeping these concerns in mind, in the following, we will sometimes refer to the confirmed structures as clusters. In particular, as discussed in Section 1, other hallmarks of a bona fide cluster include a significant population of evolved massive galaxies and a centrally concentrated distribution of galaxies. We show in Section 5.2.1 that CARLA J2039−2514 contains an overdensity of (spectroscopically unconfirmed) red galaxies with properties consistent with being passive galaxies at the redshift of the structure, and prior work by our team has demonstrated that the color-selected (i.e., red) candidate cluster members are centrally concentrated around the target RLAGN (Wylezalek et al. 2013). The overdensities reach 9.0σ and 7.8σ above the field value for the fields around MRC 2036−254 and B3 0756+406, respectively. Therefore, the balance of the evidence leans in favor of these structures being galaxy clusters/forming clusters, though a conservative approach refers to them simply as structures.

The overall redshift distribution of our two fields form a strong peak at $z \simeq 2$ (Figure 4). However, the coarse resolution of the WFC3 grism and low number statistics prevent us from inferring reliable velocity dispersions. The combined-quality A $\cup$ B$^+$ redshifts of CARLA J2039−2514 and CARLA J0800 +4029 have median redshifts of $z = 1.999$ and $z = 1.990$, respectively; the three quality A redshifts of CARLA J0800 +4029 have a median redshift of $z = 2.001$.

4.3. SFRs and Dust Extinction

Hα, one of the most reliable SFR indicators, unfortunately falls outside of the grism wavelength range at the redshift of our clusters. We therefore assume [O III]λ5007/Hα = 1 and use the Kennicutt (1983) relation, SFR $= L(\mathrm{H}\alpha)/(1.12 \times 10^{41}\,\mathrm{erg\,s^{-1}})\ M_\odot\ \mathrm{yr}^{-1}$, to convert our [O III]$\lambda$5007 fluxes into SFRs. We note, however, that there is a large scatter in the [O III]λ5007/Hα ratio reported for $z \sim 2$ star-forming galaxies. Mehta et al. (2015) indicate a linear relation between [O III]λ5007 and Hα luminosities with [O III]λ5007/H$\alpha \sim 2$ albeit with a large scatter. On the other hand, Juneau et al. (2014) suggests a [O III]λ5007/Hα ratio in the range of 0.5–1.5 for the redshift and mass of our confirmed cluster members. Using the mean [O III]λ5007 flux of our SF cluster members (8×10^{-17} erg s^{-1} cm^{-2}), but excluding the RLAGN

whose [O III] fluxes are likely enhanced by AGN photoionization, we compute a mean SFR of 20 $M_\odot$ yr^{-1} for our SF cluster members, with no dust correction applied. Given the spread in literature values for the [O III]λ5007/Hα ratio, this is considered a very crude estimate of the SFR, only considered robust at the level of a factor of two.

To better constrain our SFR lower limit, we tentatively estimate the contribution of dust extinction to the SFR. One robust method is to use the ratio of the measured Balmer decrement (the flux ratio of Hα over Hβ). However, we deem it too uncertain to use [O III]λ5007 as a proxy for Hα to calculate Balmer decrements given (1) the scatter in the [O III]λ5007 to Hα ratio, (2) the 10 times shorter wavelength baseline between Hβ and [O III]λ5007 as compared to between Hβ and Hα, and (3) the low SNR for our measured fluxes, typically of the order of five. We therefore assume a constant $A_V = 1$ mag, a typical dust attenuation in the V-band for SF galaxies (Kewley et al. 2004). Other groups have applied similar approximations (e.g., Zeimann et al. 2012; Newman et al. 2014). In particular, the level of dust extinction is expected to correlate with stellar mass, though the improvement taking that effect into account is likely small compared to the uncertainties inherent to our oxygen-based SFRs. Using the Calzetti et al. (2000) extinction curves with $R_V = 4.05$, we have $A_{[\mathrm{O\ III}]} = 0.96$ mag. Our SF cluster members, therefore, have dust-corrected SFRs in the range of $\sim$(20–140) $M_\odot$ yr^{-1}, with a median (mean) cluster member SFR[23] of $\sim$35 $M_\odot$ yr^{-1} ($\sim$50 $M_\odot$ yr^{-1}). This leads to a lower limit on the total dust-corrected SFR of $\geqslant$400 $M_\odot$ yr^{-1} for both of our clusters.

4.4. Stellar Masses

To estimate stellar masses, we scaled *Spitzer*/IRAC [3.6] and [4.5] magnitudes to Bruzual & Charlot (2003) stellar population synthesis models using a Chabrier (2003) initial mass function (IMF), single stellar population (SSP, i.e., single delta-burst population), and a $z_f = 4.5$ formation redshift. We estimate stellar masses in the range of (0.1–1.9) $\times$ 10^{11} $M_\odot$ for our CARLA cluster members (median 1.1 $\times$ 10^{11} $M_\odot$). For cluster members without CARLA counterparts, we assign upper limits of $<$10^{10} $M_\odot$ based on the IRAC depths. The RLAGN contributions to the spectral energy distributions (SEDs) likely contaminate the stellar component (e.g., Drouart et al. 2012) and overestimate the derived stellar masses. This is particularly true for type-1 AGNs like B3 0756+406, and typically less so for type-2 AGNs like MRC 2036−254. Without additional longer wavelength photometry to disentangle the stellar and AGN components in the SEDs (e.g., Seymour et al. 2007; De Breuck et al. 2010), we simply determine upper limits on the stellar masses of the RLAGN MRC 2036−254 and B3 0756+406, respectively $<3 \times 10^{11}$ and $<3 \times 10^{12}$ $M_\odot$, and we determine a limiting stellar mass $<2 \times 10^{11}$ $M_\odot$ for the CARLA J0800+4029 object #749 identified as a QSO.

4.5. Cluster Masses

We next make an estimate of the total masses of the two newly confirmed structures. The low resolution of the grism spectroscopy precludes a measurement of a velocity dispersion, and we currently lack the data to attempt other standard cluster mass measurements, such as weak lensing, diffuse X-ray emission, and SZ decrements. Therefore, we use the *Spitzer* imaging to estimate the total stellar mass in the systems, and then compare it to other, better studied clusters at comparable redshift.

Following the methodology discussed in detail in Wylezalek et al. (2014), we fit the CARLA J2039−2514 and CARLA J0800+4029 background-subtracted luminosity functions with a Schechter (1976) function, integrating over the range of ($m^\star - 2.5$) to ($m^\star + 10$). This allows us to estimate the total luminosity density of the two structures, which we convert to total stellar masses using Bruzual & Charlot (2003) solar metallicity SSP models with formation redshift $z_f = 4.5$. We assume a constant stellar mass to light ratio, determined for both the Chabrier (2003) and the Salpeter (1955) IMF. The Chabrier (2003) IMF provides total stellar masses of $M_\star = 1.9 \times 10^{12}\,M_\odot$ for CARLA J2039−2514, and $M_\star = 2.9 \times 10^{12}\,M_\odot$ for CARLA J0800+4029. We apply the same methodology to the well studied distant galaxy clusters ClG 0218.3−0510 ($z = 1.62$; Papovich et al. 2010; Tanaka et al. 2010) and IDCS J1426.5+3508 ($z = 1.75$; Stanford et al. 2012; Brodwin et al. 2016), finding total stellar masses of $M_\star = 1.2 \times 10^{12}\,M_\odot$ for ClG 0218.3−0510 and $M_\star = 1.9 \times 10^{12}\,M_\odot$ for IDCS J1426.5+3508. Our derived total stellar masses for the two new systems at $z \sim 2$ are, therefore, similar to IDCS J1426.5+3508 and slightly higher than ClG 0218.3−0510. These total masses are all $\sim$50% larger if we instead adopt the Salpeter (1955) IMF.

Tanaka et al. (2010) report an X-ray derived mass $M_{200} = (5.7 \pm 1.4) \times 10^{13}\,M_\odot$ for ClG 0218.3−0510. Brodwin et al. (2012, 2016) report a total halo mass in the range of $M_{500} = (1.9\text{–}3.3) \times 10^{14}\,M_\odot$ ($M_{200} \sim 4 \times 10^{14}\,M_\odot$) for IDCS J1426.5+3508 from a variety of halo mass tracers, including SZ, X-rays, and strong gravitational lensing (see also Gonzalez et al. 2012; and Mo et al. 2016 for a weak lensing analysis), making IDCS J1426.5+3508 the most massive galaxy cluster currently known at $z > 1.5$. Galaxy clusters in this mass range typically have stellar to halo mass ratios of a few percent (e.g., Andreon 2012; Kravtsov et al. 2014), which is consistent with our *Spitzer*-derived stellar mass estimate above. We note, however, that these relations were derived using lower redshift clusters. Based on their estimated stellar masses, CARLA J2039−2514 and CARLA J0800+4029 have comparable stellar masses to IDCS J1426.5+3508, implying that their total halo masses are likely $>10^{14}\,M_\odot$. If confirmed by additional data, this would place both structures among the most massive galaxy clusters known at $z > 1.5$.

4.6. Individual Sources

This section discusses cluster members of particular interest in detail. The full sample of cluster members is discussed in Appendix D. All spectra are shown in the same appendix.

4.6.1. CARLA J2039−2514

1. *MRC 2036−254 (#306):* this source is the targeted HzRG. It was first identified in the Molongo Reference catalog of Radio Sources (Large et al. 1981), and McCarthy et al. (1996) reported a redshift of $z = 2.0$. Both Carilli et al. (1997) and Kapahi et al. (1998)

[23] Excluding the extrema, our mean dust-corrected SFR is $\sim$40 $M_\odot$ yr^{-1}. Using the Cardelli et al. (1989) Galactic extinction law instead implies an average SFR of $\sim$60 $M_\odot$ yr^{-1} for our SF members (including the extrema).

presented radio observations of the source. The latter identified two lobes "without an unambiguously identified core," whereas the former identified three lobes, including a pair of hot spots parallel to the radio axis in the north (Overzier et al. 2005). Overzier et al. (2005) also detected an X-ray component coincident with the southwestern lobe identified in Carilli et al. (1997). In both orientations, we detect several emission lines ([O II], Hβ, [O III]), providing a redshift quality A. However, we only use the first observation to infer the source properties due to spectral overlap in the second observation. We measure a new redshift of $z = 1.997 \pm 0.004$, consistent with the previous measurement. The source IRAC color is also consistent with this redshift, as expected for an AGN (e.g., Stern et al. 2005).

2. *#306b:* the source is a previously unknown companion to the targeted HzRG, located 0.″35 to the northeast, with distinct continuum and emission lines seen offset from MRC 2036−254. The sources overlap in the second orientation, so all measurements are based on the first visit (i.e., orientation). Several lines are detected, providing a redshift of $z = 1.999 \pm 0.004$ (quality A) consistent with the HzRG. We find a slightly lower [O III] flux but a higher Hβ flux as compared to MRC 2036−254, but still with a sufficiently high line ratio to be suggestive (though not conclusive) of an AGN ($\log_{10}([\mathrm{O\,III}]/\mathrm{H}\beta) = 0.55$). MRC 2036−254 and #306b are likely a merging system[24], perhaps a dual AGN, whose components are separated by 3 kpc. With this close separation, we take the conservative approach and do not list #306b as an isolated additional galaxy in the cluster, but instead consider the system to be a single galaxy at the redshift measured for MRC 2036−254.

4.6.2. CARLA J0800+4029

1. *B3 0756+406 (#371):* this source is the targeted QSO. It was first identified in the new Bologna sky survey (Ficarra et al. 1985), and its redshift ws determined at $z = 2.021$ in SDSS Data Release 7 (DR7, Schneider et al. 2010), albeit with some scatter across various SDSS analyses: Hewett & Wild (2010) reported $z = 2.014$ based on their improved redshifts for 91,000 quasar spectra from SDSS DR6, while SDSS DR2 reported $z = 2.026$ (Abazajian et al. 2004). We did not reliably identify broad lines in the G141 spectra. Therefore, we re-observed the target at Palomar Observatory (see details in Section 2.3.2). From several emission lines (Lyα, C IV, C III], and Mg II), we measure a new redshift of $z = 2.004 \pm 0.002$ (quality A), slightly lower than its previous lower-quality SDSS redshift. The source has an IRAC color consistent with this redshift, as expected for an AGN.
2. *#372:* the first observation of this galaxy is contaminated by the target quasar, B3 0756+406, but we obtain $z = 2.001 \pm 0.004$ from the second observation. We detect a break around 12000 Å, consistent with a D4000 break at the redshift measured from [O III].[25] Hβ is tentatively detected slightly below our detection limit. Therefore, we assign a quality A to the redshift based on the detections of [O III]λ5007 and the D4000 break. The detections indicate that this source possesses both old and young stellar populations, and an active star-forming region. This source is located $\sim$3″ to the northeast of B3 0756+406, implying a separation of $\sim$25 kpc from the QSO (see Appendix D).
3. *#749:* the second observation is contaminated over the full wavelength range, save for some pixels around 15000 Å, which only allow us to confirm the presence of emission lines seen in the first observation. Our flux measurements come from the first observation, and we measure both strong [O III] and Hβ emission. We measure a redshift of $z = 2.001 \pm 0.004$ (quality A). The source IRAC color is consistent with the measured redshift. This source shows broad Hβ, narrow [O III], and a tentative [Ne III] emission lines, as seen in Appendix D, which likely identifies this source as a QSO, even though we do not totally exclude that the poor G141 resolution might possibly bias its identification as an AGN.

5. DISCUSSION

5.1. Method Efficiency

The two $z = 2$ structures reported in this paper likely represent some of the highest redshift clusters currently spectroscopically confirmed. They illustrate the high efficiency of our approach to target RLAGN with IRAC mapping and *HST* grism follow-up. Because the two fields are only a pilot study for our full sample of 20 cluster candidates, we next explore the efficiency of our grism spectroscopy and [3.6]–[4.5] selection.

5.1.1. Grism Efficiency

We assess in this section the outcome of our *HST* observations. In Figure 6, we show the flowchart of the classification of *HST* sources from our master catalog. The classification is shown for both fields, with the numbers on the left side of each box corresponding to the MRC 2036−254 field and the numbers on the right side corresponding to the B3 0756+406 field. We also display in parentheses numbers corresponding to the classification for secure *Spitzer* color-selected candidates that have a single *HST* counterpart. Overall, we determine redshifts for 6% of our exploitable *HST* sources (31/550 and 26/452, respectively, for the fields around MRC 2036−254 and B3 0756+406); where "exploitable" is defined to mean that >75% of the source continuum falls on the detector and contamination is less than 60% of the cutout length. We find that 2% of sources (9/550 and 10/452) are confirmed cluster members—i.e., for every three redshifts that we measure, we find one cluster member. This is consistent with probing a biased environment, and is not an instrumental bias. For example, the redshift distribution of the 3D-*HST* field survey (Momcheva et al. 2015) is roughly flat in the same

[24] Note that type-2 RLAGN are often found to be associated with close merging systems (e.g., Chiaberge et al. 2015).

[25] Even though we extracted the 1D spectrum of the second observation from a contaminant-free region, we cannot totally exclude that the bright nearby continuum seen on the 2D cutout might be partly causing the D4000 break-like feature in the source continuum.

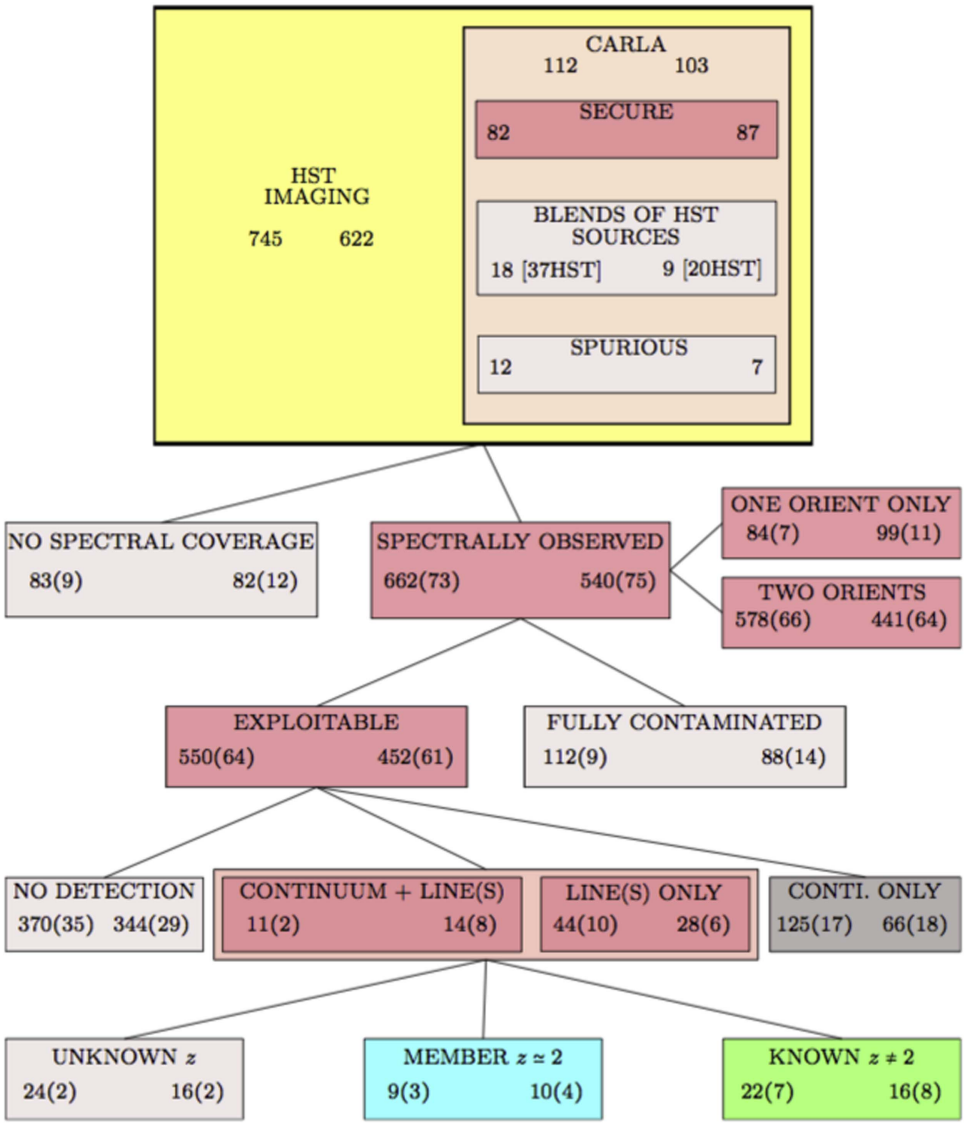

Figure 6. Flowchart of the classification of all sources from our master catalog. Inside each box, left side numbers correspond to the MRC 2036−254 field whereas the right side numbers correspond to the B3 0756+406 field. Numbers in parentheses refer to secure CARLA sources—i.e., non-spurious *Spitzer* color-selected sources with a single *HST* counterpart. In total, we confirmed 9 and 10 cluster members for CARLA J2039−2514 and CARLA J0800+4029, respectively. Three and four of the members were selected as CARLA sources, respectively.

redshift window ($0.7 < z < 2.3$), based on their sample of 46, 256 grism redshifts in this window obtained over 626 arcmin^2 with a similar two-orbit per field *HST* grism program. Of the exploitable *HST* sources, 71% (370/550 and 344/452) are not detected in the dispersed grism data. Moreover, of the sources with spectral detections, 66% (125/180 and 66/108) show continuum only, for which we could not measure a redshift because no emission lines were detected. These sources are likely a mixture of: (1) stars, (2) old and passive (quiescent) galaxies with little star formation, (3) galaxies at redshifts for which no strong features are covered by our grism observations, and (4) SF galaxies for which we do not detect emission lines at the depth of our data (SFR $\lesssim$20 $M_\odot$ yr^{-1}, unless highly dust-obscured). Also, we have not been able to determine a redshift for 40% (24/55 and 16/42) of sources with detected emission line(s) (with or without continuum) because of the ambiguity of the nature of the line (s). This number improves by a factor of 3.5 when considering *Spitzer* color-selected sources since we have color information that helps identify ambiguous emission lines. Overall, we also lose 26% (195/745 and 170/622) of the source spectra because of full contamination of their spectral first orders (15%, 112/745 and 88/622) or because their traces fell outside of the G141 detector (12%, 83/745 and 82/622).

5.1.2. IRAC Color-selection Efficiency

The primary aim of our *HST* program is to confirm galaxy clusters that were selected as overdense fields of mid-infrared color-selected galaxies. Hence, we also evaluate the success of the CARLA selection method given our *HST* observations. Focusing on the numbers in parentheses in the flowchart, we also find that a large fraction, 51% (35/64 and 29/61, respectively, for the fields around MRC 2036−254 and B3 0756+406) of the exploitable CARLA sources do not have any spectroscopic detection at the depth of our grism observations. This is better than the 71% of all *HST* sources, implying that CARLA sources are brighter, on average, than

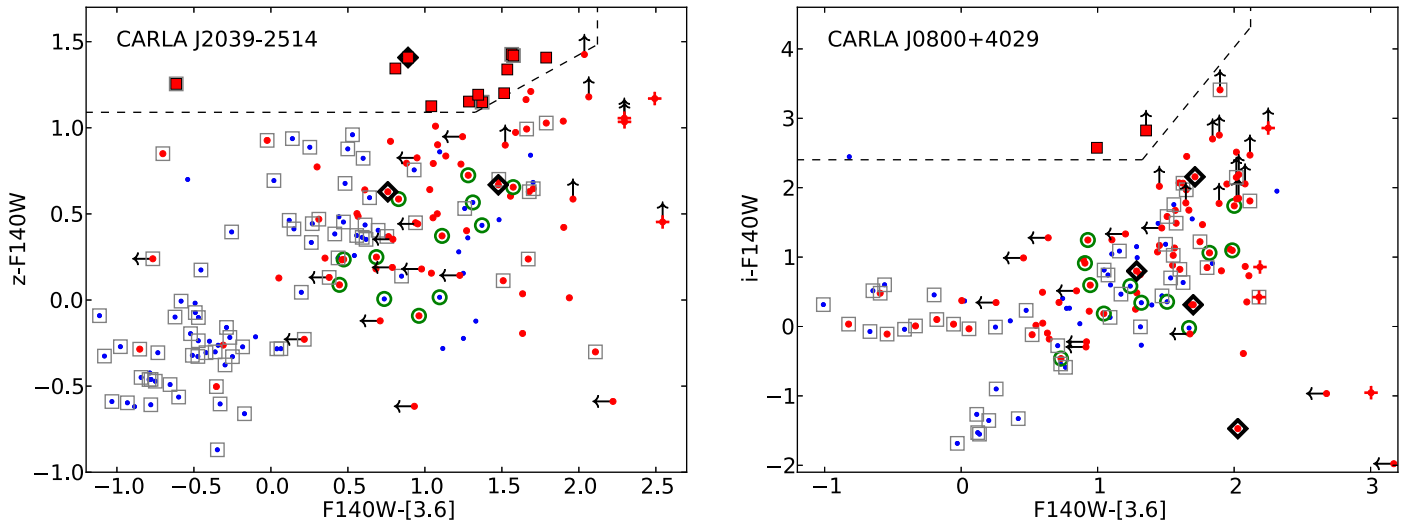

Figure 7. Color–color diagrams of CARLA J2039−2514 (left) and CARLA J0800+4029 (right). The dashed lines, adapted from Williams et al. (2009) as described in Section 5.2, separate passive, dusty SF, and SF galaxies. Passive galaxies are located inside the upper left quadrant and dusty SF galaxies are on the right side of the quadrant vertical boundary. All CARLA candidates are shown by red markers, with the passive CARLA candidates highlighted by red squares and the dusty SF CARLA candidates by red plus "+" signs; bluer sources with IRAC colors <-0.1 mag (AB) are shown by solid blue circles. Black diamonds highlight confirmed cluster members, and green rings are spectroscopically confirmed non-members. Open gray squares indicate continuum-only sources as identified in the grism data. Leftward arrows denote sources below our detection limit at 3.6 μm, and upward arrows in the optical (2σ); their positions in the color–color plane are set using these limits.

our *HST* sources. This is unsurprising since rest-frame near-infrared luminosity strongly correlates with stellar mass (e.g., Gavazzi et al. 1996), and our IRAC 4.5 μm flux cut imposes a limiting stellar mass around $1 \times 10^{10}\,M_{\odot}$ on the CARLA sources, whereas the *HST F*140*W* imaging also detects sources below the IRAC flux limit.

We determine the redshift of 18% (10/64 and 12/61) of the exploitable *Spitzer* color-selected sources, and we find that 6% (3/64 and 4/61) are cluster members. Again, we identify one cluster member for every three sources with redshift determinations. Among the CARLA sources with spectral detections, 57% (17/29 and 18/32) show continuum without detectable emission lines. This suggests a large fraction of quiescent galaxies and/or galaxies with low or dust-extincted SFRs as potential cluster members (see Section 5.2). Note the similarity with Brodwin et al. (2013), albeit at lower redshift, who found that ∼40% of cluster members at $1.37 < z < 1.50$ are SF galaxies based on the *Spitzer* 24 μm emission, using an infrared-selected sample with stellar masses $>10^{10.1}\,M_{\odot}$, and a SFR lower limit of $50\,M_{\odot}\ \mathrm{yr}^{-1}$ for the SF members. This is also consistent with the work of Cooke et al. (2016), who found that 76% of CARLA galaxies ($M > 10^{10}\,M_{\odot}$) in the field of CARLA J1753+6311 ($z = 1.58$) are quiescent. The CARLA selection method therefore finds both passive galaxies and SF galaxies, though the shallow grism data presented here are only capable of confirming the latter.

5.2. Stellar Populations

Williams et al. (2009; see also Labbé et al. 2005; Wuyts et al. 2007; Whitaker et al. 2011) have shown that it is possible to use rest-frame *UVJ* colors to separate the SF, dusty SF, and passive populations. To build our color–color diagrams (Figure 7), we use observed $z/i - F140W$ versus $F140W$ – [3.6]. Following Mei et al. (2009) and using Mei's codes and the python version of `EZGAL` (Mancone & Gonzalez 2012), we transform Williams et al. (2009) color limits into our observed apparent colors. We use a Bruzual & Charlot (2003) SSP model with galaxy formation redshifts averaged between $z_f = 3$ and 8, and metallicities equal to 40% solar, solar, and 2.5 times solar; and we age the templates to $z = 2$. We average the color conversions using a set of formation redshift ranges from $z_f = 3$–8 to $z_f = 5$–8 increasing by steps of 0.1. This is a conservative simple model and assumes that passive galaxies are mostly located close to the passive boundary defined in Williams et al. (2009). A more detailed analysis of the CARLA cluster stellar population will be performed in future work.

In Figure 7, we plot color–color diagrams for the two fields to investigate the presence of passive cluster members associated with CARLA J2039−2514 and CARLA J0800+4029, and in Figure 8 we plot their color–magnitude diagrams (CMDs). We use *i*-band data from Cooke et al. (2015) for CARLA J0800+4039 and a 4800 s *z*-band image obtained with VLT/ISAAC on UT 2002 July 17 for CARLA J2039−2514.[26] For both CMDs, we use *HST*/*F*140*W* data to bracket the D4000 break at $z = 2$. In the color–color diagrams, the passive candidates are located inside the upper left quadrant. The SF population is located below the horizontal line, whereas dusty SF galaxies lie on the right of the vertical boundary. We identify 14 passive galaxies for CARLA J2039−2514 (2 of them outside the plot) and 2 for CARLA J0800+4029.

5.2.1. Density of Passive Candidates

We compare the density of passive, red ($([3.6]-[4.5])_{\mathrm{AB}} > -0.1$), sources in our RLAGN fields with densities of sources similarly selected in wide-field surveys. We make use of the 3D-*HST* multi-wavelength catalogs (Skelton et al. 2014) in the five CANDELS fields (GOODS-North, GOODS-South, AEGIS, COSMOS, and UDS; Grogin et al. 2011). All CANDELS fields were at least partially covered by *i*-band,

[26] Archival data from run ID 69.A-0234.

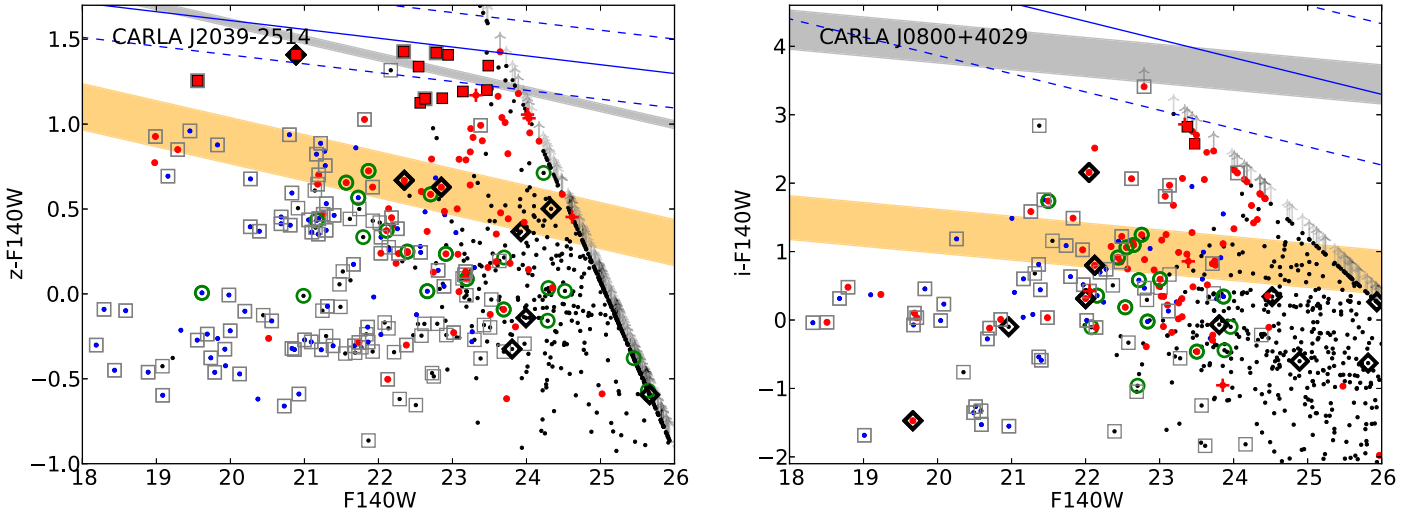

Figure 8. Color–magnitude diagrams of CARLA J2039−2514 (left) and CARLA J0800+4029 (right). Same markers as in Figure 7, with the addition of sources detected in the optical and $F140W$ but not detected in IRAC shown by small black dots. Sources below our optical detection limits (2σ) are set to these limits and shown with upward arrows. The gray and orange shaded areas represent estimates of a $z = 2.0$ red sequence for delta-burst and exponentially decaying stellar populations, respectively, described in Section 5.2.2. The thicknesses of these regions correspond to formation redshifts in the range of $z_f = 3.0$–8.0. The solid blue lines represent the $z = 1$ Mei et al. (2009) color–magnitude relation passively evolved to $z = 2.0$, as described in Section 5.2.2 (the dashed blue lines represent the 3σ range).

z-band, $F140W$, 3.6, and 4.5 μm observations. The $F140W$ images have the most limited coverage; we therefore use the $F140W$ image field of view to derive source densities (Brammer et al. 2012). We isolate passive, red (i.e., CARLA), sources using the same color-selections as described above. At the depth of our RLAGN field data, we expect approximately nine sources (1.69 ± 0.04 arcmin^{-2}) selected by the $z/F140W/[3.6]$ criterion in the 5.38 arcmin^2 *HST* field of view of CARLA J2039−2514, and approximately two sources (0.38 ± 0.02 arcmin^{-2}) selected by the $i/F140W/[3.6]$ criterion in the 5.54 arcmin^2 *HST* field of view of CARLA J0800+4029. We identify 14 (∼2.6 arcmin^{-2}) and 2 (∼0.4 arcmin^{-2}) passive CARLA candidates for CARLA J2039−2514 and CARLA J0800+4029, respectively. CARLA J2039−2514 is therefore consistent with possessing an overdensity of $z \sim 2$ passive red galaxies relative to the field, while our comparison suggests that CARLA J0800+4029 has similar values than the field. However, these are likely underestimates of the true (over)densities given the limiting magnitudes in the CARLA imaging of those fields.

5.2.2. Red Sequences and SF Populations

In the CMDs (Figure 8), the orange and gray shaded areas show estimates of the expected color of L^* early-type galaxies computed with a Bruzual & Charlot (2003) passive evolution model of solar metallicity and a Salpeter (1955) IMF.[27] These were calculated using the python version of EZGAL (Mancone & Gonzalez 2012) with the appropriate filter transmission curves. We evolve an SSP (i.e., delta-burst), shown by the gray shaded areas, and an exponentially decaying stellar population of characteristic timescale $\tau = 1$ Gyr, shown by the orange shaded areas. The thickness of these regions correspond to formation redshifts over the range $3 < z_f < 8$. Both model evolutions are normalized to match the typical CARLA L^* at $z = 2.0$ (Wylezalek et al. 2014), and assume slopes of −0.1, similar to what is observed in the Coma cluster at similar rest-frame wavelengths (Eisenhardt et al. 2007). To compare with the color–magnitude relation (CMR) observed in confirmed X-ray and infrared detected clusters at redshift $z \sim 1$, we plot the Mei et al. (2009) early-type CMR (solid blue lines; the blue dashed lines show the 3σ dispersion around the mean) evolved passively to $z = 2$. Following Mei et al. (2009), we use a Bruzual & Charlot (2003) SSP model with galaxy formation redshifts between three and eight, and metallicities equal to 40% solar, solar, and 2.5 times solar, to convert rest-frame $(U - B)$ versus M_B derived at $0.8 < z < 1.3$ to our observed bandpasses at $z = 2$. We again average the color conversions using a set of ranges from $z_f = 3$–8 to $z_f = 5$–8. The Mei et al. (2009) early-type galaxy CMR parameters are derived using *HST*/ACS filters that correspond to rest-frame $(U - B)$ and M_B in the range $0.8 < z < 1.3$. While the z-band and $F140W$-band correspond to the same rest-frame for CARLA J2039−2514, the i-band probes bluer stellar populations than the U-band rest-frame. Within the uncertainties, these relations are consistent with the predictions from Bruzual & Charlot (2003).

The majority of CARLA J2039−2514 passive candidates identified in Figure 7, with $z - F140W \gtrsim 1$ mag and $F140W > 20$ mag, agree well with the SSP models shown on the CMD (Figure 8), suggesting CARLA J2039−2514 hosts a population of quiescent galaxies consistent with a cluster red sequence at $z = 2.00$. On the other hand, CARLA J0800+4029, unlike CARLA J2039−2514, does not exhibit $F140W < 23$ mag passive candidates consistent with a cluster red sequence, and the depth of our i-band data prevents us from confirming $F140W > 23$ mag sources for this field. Specifically, 13 sources (marked with upward arrows in Figures 7 and 8) do not have i-band detections and therefore require deeper data to determine whether they are passive candidates populating what could constitute a nascent cluster red sequence. In each color–color diagram, we only identify a handful of dusty SF CARLA candidates, none of which are spectroscopically confirmed as members or non-members. All spectroscopically confirmed members and non-members are identified as SF galaxies in the color–color diagrams, as

[27] Using a Chabrier (2003) IMF instead does not significantly change the results.

expected, with the exception of the target RLAGN in CARLA J2039−2514, which falls in the passive region as expected for a type-2 RLAGN. Four of the confirmed members of CARLA J2039−2514 seem to be well described by the exponentially decaying model of star formation. The remaining two members that have both F140W and z-band detections, and most of the confirmed members of CARLA J0800+4029 do not seem to agree with this model, suggesting that the build-up of their stellar content followed a diversity of star-formation histories (SFHs). This supports Cooke et al. (2015) who showed that the SFHs of CARLA cluster galaxies are best described by multiple bursts of star formation normally distributed over a few gigayears, or distributed following the cosmic SFH. Exploration of a range of SFHs is, however, beyond the scope of this paper and will be addressed in future work. Finally, we note that only one blue ($([3.6]-[4.5])_{AB} < -0.1$ mag) source falls in the passive region of the color–color diagrams, and that the putative red sequence of CARLA J2039−2514 almost exclusively comprises a population of quiescent galaxies up to $F140W < 24$ mag. The spectroscopic confirmation of these passive CARLA candidates, however, will require significantly deeper data.

5.3. Comparison to Other High-redshift Clusters

We compare our results to other high-redshift clusters spectroscopically confirmed using *HST*/WFC3 grism data. Gobat et al. (2013, hereafter G13), reported on a rich cluster at $z \simeq 2$. They first reported evidence of a fully established galaxy cluster at $z = 2.07$ (Gobat et al. 2011) from X-ray emission, ground-based spectroscopy, and ground- and space-based photometry, later revised by G13 to a slightly lower redshift using deep *HST* grism observations. The system consists of two unrelated aligned structures, with the background overdensity being "sparse and sheet-like." The G13 median redshift of the *HST*/WFC3 confirmed members of the foreground overdensity is $z = 1.993$, with a standard deviation of 0.012. With median redshifts of $z = 2.000$ (standard deviation 0.005) and $z = 1.986$ (standard deviation 0.014), CARLA J2039−2514 and CARLA J0800+4029, respectively, are among the most distant confirmed clusters currently known. G13 confirmed 22 members with 18 orbits and three orientations (12.5 hr on source) including five quiescent sources, and found no evidence for an already formed red sequence within 20″ of the cluster core (Gobat et al. 2011). More recently, Newman et al. (2014), hereafter N14, confirmed another rich cluster at high redshift using *HST*/WFC3 slitless spectroscopy. With 14 orbits, they confirmed 19 members at $z = 1.80$, of which more than 75% are quiescent. They found a clear red sequence of observed mean color $\langle z - J \rangle = 1.98 \pm 0.02$, which includes 13 of their 15 quiescent cluster members. Zeimann et al. (2012, hereafter Z12), also confirmed both emission-line and quiescent sources in a cluster at $z = 1.89$ using six orbits of *HST*/WFC3 grism spectroscopy. Z12 showed that a significant fraction of early-type galaxies in the cluster field were consistent with forming a red sequence. These deep observations show that clusters can host a substantial fraction of quiescent galaxies even at early epochs. By design, our shallow two-orbit per field strategy only confirms SF members. In addition to the confirmed emission-line members, we find a large fraction (79%, 52/64, and 47/61) of *Spitzer* color-selected cluster candidates below our detection limit or showing continuum only. CARLA J2039−2514 and CARLA J0800+4029 are therefore relatively robust confirmations, and have a high potential for being richer structures than what our shallow *HST* observations allowed us to unveil. Furthermore, we note that our two-orbit strategy spectroscopically confirms approximately five cluster members per orbit, which is approximately four times more efficient than the >10-orbit programs reported in G13 and N14.

From X-ray emission and richness, G13 estimated a mass of $M_{200} \sim 5 \times 10^{13}\, M_\odot$ for their cluster. N14 reported a massive cluster with $M_{200} = (2\text{–}3) \times 10^{14}\, M_\odot$, including five very massive members whose stellar masses are in the range of $(4\text{–}10) \times 10^{11}\, M_\odot$. We do not find such high masses for our confirmed cluster members (with the exception of the RLAGN); our 7 IRAC-detected sources have a median stellar mass of $1.1 \times 10^{11}\, M_\odot$, and the remaining 12 non-IRAC detected members have masses $<10^{10}\, M_\odot$. Z12 derived SFRs from the [O II] and Hβ lines and find SFRs in the range of (20–40) $M_\odot$ yr^{-1}. Based on the admittedly crude [O III] SFR indicator, we find similar SFRs for 9/16 of our SF cluster members. We also find higher SFRs, in the range of (40–140) $M_\odot$ yr^{-1}, for a significant number of SF cluster members (7/16). Note that our line detection limit imposes an SFR lower limit of $>20\, M_\odot$ yr^{-1} (similar to Z12 but based on a different line). According to the SFR/stellar-mass relation in Rodighiero et al. (2011) for $1.5 < z < 2.5$ galaxies, our low-mass cluster members (typically all the non-IRAC detected members, with masses $\lesssim 10^{10}\, M_\odot$) are above the star-forming main-sequence toward starburst galaxies. Our detection limits prevent us from confirming main-sequence galaxies at these masses and redshifts.

In Section 4.3, we showed that confirmed emission line members of both structures imply total cluster SFRs of at least $\sim 400\, M_\odot \mathrm{yr}^{-1}$ within ~500 kpc of the cluster centers, which are assumed to be coincident with the target RLAGN. Based on *Spitzer* 24 μm imaging of a sample of clusters from the *Spitzer*/IRAC Shallow Cluster Survey, Brodwin et al. (2013) showed a steeply increasing SFR in cluster cores out to $z = 1.50$, with an average SFR of several hundred $M_\odot$ yr^{-1} found in the cores of the highest redshift clusters in that study. Alberts et al. (2014, 2016) find similar results based on longer wavelength *Herschel* data of a similar cluster sample. The results found here at $z \sim 2$ for CARLA J2039−2514 and CARLA J0800+4029 are consistent with those studies, though higher fidelity SFR indicators for these newly confirmed structures would be highly preferable to the current [O III]-based values.

Although G13 found no evidence for an already formed red sequence within 20″ of the cluster core, they determined, from their best subsample of (96) cluster candidates comprising 14 spectroscopic members and 82 photo-z candidates (expected to include 50 interlopers), that ~(60–80)% of candidates within ~20″ of the cluster core are passive regardless of mass, compared to ~20%, ~40%, and ~60% in the field for $\log M/M_\odot > 10$, 10.5, and 11, respectively (Strazzullo et al. 2013). We additionally note that the structure reported in Spitler et al. (2012) and Yuan et al. (2014), respectively, discovered at $z = 2.2$ from photometric redshifts and later spectroscopically confirmed at $\langle z \rangle = 2.095$ with 57 members, comprises several 1′ radius overdense groups covering a 12′ × 12′ area in COSMOS (Scoville et al. 2007). This structure has a slightly enhanced number of red galaxies for two groups compared to the field, with $N_{red} = 0.5 \pm 0.2 \times N_{tot}$ compared to 0.2 ± 0.03 in the field. Our results are also indicative of the presence of passive

CARLA candidates associated with CARLA J2039−2514, while CARLA J0800+4029 exhibits a number of passive candidates similar to the field in our comparison. A careful analysis accurately evaluating the passive fraction of galaxies in our structures will be addressed in E. A. Cooke et al. (2016, in preparation).

6. SUMMARY

We conclude the following from our *HST*/WFC3 *F*140*W* and G141 follow-up observations on two overdense CARLA fields, which are the first two of a sample of 20 cluster candidates at $1.4 < z < 2.8$.

1. We spectroscopically confirm two *Spitzer* color-selected overdensities as high-redshift structures. Adopting the Eisenhardt et al. (2008) criteria defining a $z > 1$ galaxy cluster through spectroscopic confirmation, these two structures are among the most distant clusters currently known. Furthermore, though we note that the Eisenhardt et al. (2008) criteria may also identify sheets, filaments, groups, and protoclusters when applied to grism data, the structures reported here possess additional attributes typically used to identify galaxy clusters: CARLA structures are, on average, centrally concentrated, and CARLA J2039−2514 has an overdensity of red galaxies consistent with being passive cluster members. Our results suggest that CARLA J2039−2514 is a bona fide galaxy cluster. While CARLA J0800+4029 conforms to the Eisenhardt et al. (2008) criteria, has a centrally concentrated 7.8σ overdensity of *Spitzer* color-selected (i.e., red) candidate cluster members, and has comparable stellar mass to the most massive cluster known to date at $z > 1.5$, it lacks a clear overdensity of passive candidates and a red sequence population in the current data, suggestive of a younger forming cluster.
2. We identify CARLA J2039−2514 at $\langle z \rangle = 1.999$ (median $z = 2.000$), consisting of 9 confirmed members, including a potential dual AGN. We also identify CARLA J0800+4029 at $\langle z \rangle = 1.986$ (median $z = 1.986$), consisting of 10 confirmed members including 2 quasars. We estimate median (mean) SFRs of $\sim 35\ M_\odot\ \mathrm{yr}^{-1}$ ($\sim 50\ M_\odot\ \mathrm{yr}^{-1}$) and average stellar masses of $\lesssim 1 \times 10^{11}\ M_\odot$ for the confirmed star-forming members of both CARLA J2039−2514 and CARLA J0800+4029.
3. Considering the total background-subtracted mid-infrared light from the two structures, we find that the inferred total stellar masses are comparable to the most massive clusters known at slightly lower redshift ($z \sim 1.7$). This analysis crudely implies that these structures have total masses of $M_{500} \sim 10^{14}\ M_\odot$.
4. With just two orbits, we only confirm emission-line sources with SFRs $> 20\ M_\odot\ \mathrm{yr}^{-1}$. We show that *HST* grism spectroscopy is efficient at confirming galaxy clusters at high redshift even with shallow observations, but that deeper spectroscopic data is required to confirm the clusters' passive population.
5. We study the two cluster CMRs. While CARLA J2039−2514 shows a population of red and quiescent galaxies where we would expect a red sequence at these redshifts, CARLA J0800+4029 does not exhibit such a population up to $F140W < 23$ mag. However, a promising 13 red CARLA J0800+4029 sources with $F140W > 23$ mag require deeper optical imaging to determine whether they are passive candidates and populating a nascent cluster red sequence. We conclude that CARLA J2039−2514 already hosts a population of quiescent galaxies, with little contamination from obscured star-forming galaxies.
6. We show that our CARLA selection is robust. It efficiently selects overdense fields at high redshifts while potentially selecting at the same time the most likely detectable emission-line sources. Our *Spitzer* mid-infrared color selection increased the source likelihood of being a cluster member by a factor of three compared to no color selection in these biased environments.
7. Our low-resolution observations have redshift uncertainties of up to 1000 km s^{-1}. Higher resolution spectroscopy will be required to reliably measure velocity dispersions and cluster masses. Future observations could also provide accurate SFRs for our cluster members using more robust estimators such as Hα luminosities and far-infrared observations, and better determine stellar masses using additional photometric data.

We thank our anonymous referee for comments and suggestions that improved the quality of this paper. This work is based on observations made with the NASA/ESA *Hubble Space Telescope*, obtained at the Space Telescope Science Institute, which is operated by the Association of Universities for Research in Astronomy, Inc., under NASA contract NAS 5-26555. This work is also based in part on observations made with the *Spitzer Space Telescope*, which is operated by the Jet Propulsion Laboratory, California Institute of Technology, under a contract with NASA. This work is also based in part on observations made with the 200 inch Hale Telescope, Palomar Observatory, operated by the California Institute of Technology. D.W. acknowledges support by Akbari-Mack Postdoctoral Fellowship. S.M. acknowledges financial support from the Institut Universitaire de France (IUF), of which she is senior member. E.A.C. acknowledges the support of the STFC. N.A.H. acknowledges support from STFC through an Ernest Rutherford Fellowship.

Facilities: *HST* (WFC3, STScI), *Spitzer* (IRAC, JPL/Caltech), Palomar (DBSP, Caltech).

APPENDIX A
NOTES ON DATA PROCESSING

A.1. FLT Files

Three different kinds of calibrated data can be retrieved from MAST: "calibrated, flat-fielded individual exposures" (FLT), "calibrated, cosmic-ray-rejected, combined images" (CRJ), and "calibrated, geometrically corrected, dither-combined images" (DRZ; WFC3 Data Handbook, Rajan et al. 2010). According to the handbook, the `Astrodrizzle` package of the aXe software for slitless spectroscopy data extraction (Kümmel et al. 2009) supersedes the CRJ and DRZ data preparations of the standard WFC3 calibration program (`calwf3`). Therefore, we only retrieved FLT files, which are used as input by aXe.

A.2. Image Combination and Source Extraction

We first used the aXe (v2.4.4) `astrodrizzle` task to combine the eight *F*140*W* dithered direct exposures of each field (four from each orientation). This step creates a deep

(1023–1073 s) drizzled direct image with bad pixels and cosmic rays rejected. The combined direct images of each field are shown in Figure 3, with the positions of confirmed cluster members indicated.

In order to associate sources and spectra and to wavelength calibrate the spectra, we first create a catalog of sources in each field using SExtractor (Bertin & Arnouts 1996) on the drizzled image. We create a deep catalog using SExtractor detection parameters selected to identify even the faintest sources (DETECT_MINAREA = 4, DETECT_THRESH = 2, and ANALYSIS_THRESH = 2). Lower values only add spurious detections (e.g., noise clumps, stellar diffraction spikes, dismemberment of extended sources) while higher values miss a significant number of faint sources. This deep catalog, gathering information on source positions, magnitudes, sizes, and orientations, is then cleaned by hand from spurious detections. We also generate a more conservative catalog using DETECT_MINAREA = 10, DETECT_THRESH = 3, and ANALYSIS_THRESH = 3 to restrict the number of detections for the grism sky background subtraction (see Appendix A.4).

A.3. HST–CARLA Cross-correlation

We cross-correlate our *HST* and CARLA/*Spitzer* catalogs for two reasons. First, we update the nature of the CARLA sources themselves. With nearly 10 times better spatial sampling than *Spitzer*, *HST* provides morphological information and identifies some IRAC sources as spurious detections or blends, potentially leading to misfigured IRAC colors and erroneous CARLA selection. Second, we wish to investigate the spectra of all CARLA sources in our grism data. To the cleaned deep catalog, we add *Spitzer* CARLA candidates too red to be detected in the *HST* direct imaging. Even though these undetected sources may not show any continuum, they can potentially show emission lines in the grism data. This step required a slight astrometric correction ($\sim 0\farcs2$) to the IRAC positions. We based our correction on secure CARLA sources identified in the first step. At this point, we now have our cleaned, complete and final catalog of sources for spectroscopic analysis, referred to as the master catalog.

A.4. Back Projection and Background Subtraction

Exposure blocks (pairs of direct and grism observations) are slightly offset from one another. Therefore, we cannot directly associate the master catalog sources to their spectra. Using the `Astrodrizzle` aXe task `iolprep`, we then project back the master catalog to each individual direct image and obtain individual catalogs corresponding to each grism exposure, required for stacking the grism data of each observation.

Prior to stacking the grism data, we remove the overall background level of the G141 detector, which varies significantly along its surface ($\sim$(0.9–2.4) e^- s^{-1}). The aXe task `axeprep` scales a master sky background on spectral-free regions. We use the shallow catalog, projected back to individual frames, as our master catalog is too deep for aXe to produce enough sky-free regions.

A.5. Contamination Models

Two kinds of contamination models can be generated using the aXe task `axecore`: quantitative or qualitative. For each source, the quantitative contamination model produces a 2D cutout of the first order grism spectrum, and shows how many potential contaminating spectral traces from other sources fall in the cutout. However, this model is purely geometrical and includes all spectral orders from all sources regardless of their likelihood of actually being detected. This leads to large overestimation of the contamination and typically no contaminant-free regions. On the other hand, the qualitative contamination model computes the shapes and flux intensities of the spectral traces, based on position, magnitude, and size of the sources. One can choose between the "Gaussian" and the "fluxcube" methods (described in the aXe User Manual (v2.3), Kümmel et al. 2011). Briefly, the "Gaussian" method approximates the shapes of sources as Gaussians and requires magnitudes from at least one band to estimate flux intensities (more bands provide better estimates). The "fluxcube" method creates more realistic spectral trace shapes as it models the morphologies of the sources from at least one *HST* image and a segmentation map (again, more images from multiple bands provide better estimates). Gobat et al. (2013) report that the "fluxcube" method is often a poor approximation of the spectrum, even with several multi-band *HST* images available. With only *F*140*W* available to us, we use the "Gaussian" method to locate traces and zeroth orders of possible contaminants.

APPENDIX B
CLUSTER MEMBER PROPERTIES

We present in Table 3 the properties of the members of our two clusters, CARLA J2039−2514 and CARLA J0800+4029.

APPENDIX C
NON-CLUSTER MEMBER EMISSION LINE SOURCES

We present in Table 4 the measured redshifts of non-cluster member sources in the fields of view of our clusters.

APPENDIX D
INDIVIDUAL SOURCES

We discuss here the spectra and properties of all cluster members, except the ones already discussed in Section 4.6. We also show the 2D cutouts, 1D spectra, fitting and contamination contours of all cluster members, as well as their direct image stamps (Figure 9).

D.1. CARLA J2039−2514

1. *#119:* We identify contamination above 15200 Å and below 11500 Å in the first observation, and up to 15200 Å in the second observation, albeit slightly offset from the center of the 2D extraction. This *Spitzer*-selected CARLA source has a mid-infrared color consistent with the emission line seen in both orientations as being [O III]. We measure a redshift of $z = 1.987 \pm 0.007$, and we do not detect Hβ or other emission lines. Hence, we assign a quality B$^+$ to the redshift based on the emission line and *Spitzer* color.
2. *#174:* The contamination model for this *Spitzer*-selected CARLA source does not identify strong spectroscopic contamination. However, the two emission-like features seen at 14100 and 14600 Å in the first observation are not observed in the second observation. This suggests unidentified contamination at the level of our contamination contours. This could be due to pixel noise, a non-

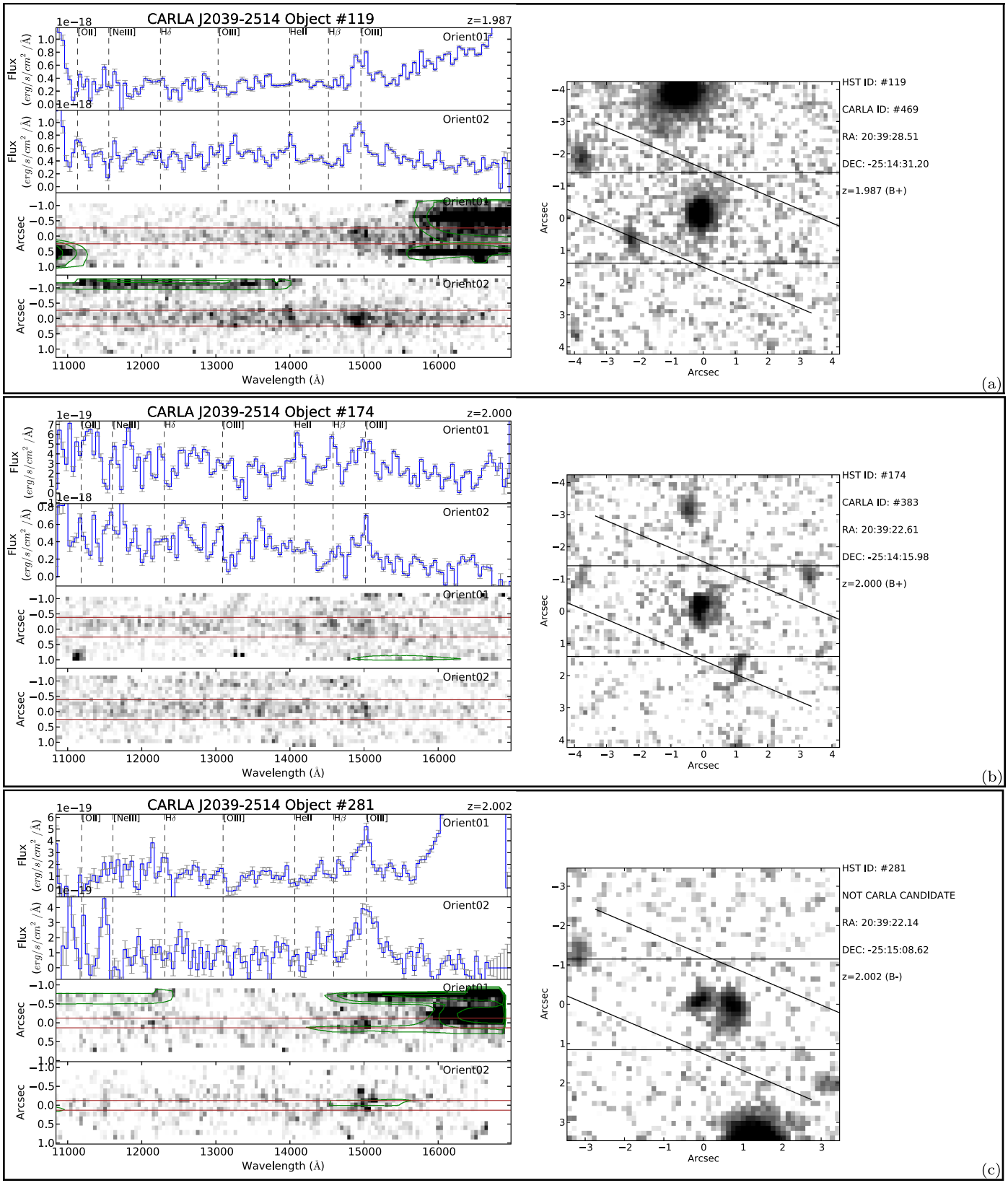

Figure 9. Cutout spectra in 2D and 1D and direct imaging of all cluster members, for both fields. The slits in the direct imaging represent the dispersion direction and width of the 2D spectral cutouts, where the horizontal slit correspond to the first observation, and the inclined one to the second. The red slits in the 2D images, however, represent the width from which we extract the 1D spectra. Gray scales are arbitrary set to visually facilitate the identification of the source spectral features. The vertical dotted lines are visual aids locating possible emission lines at the measured redshifts of each source. The green contours represent the contamination model contours as described in Sections 3.2 and 3.3.2. The gray error bars on top of the 1D spectra represent the grism 1σ wavelength-depend background noise. Panels (a)–(j) correspond to CARLA J2039−2514, panels (k)–(t) to CARLA J0800+4029. Note that the 2D cutouts of #306b do not show any contamination model contours since we re-extracted this source alone, however, we invite the reader to have a look at #306 (Panel (d)) since the two sources are present on the same cutout.

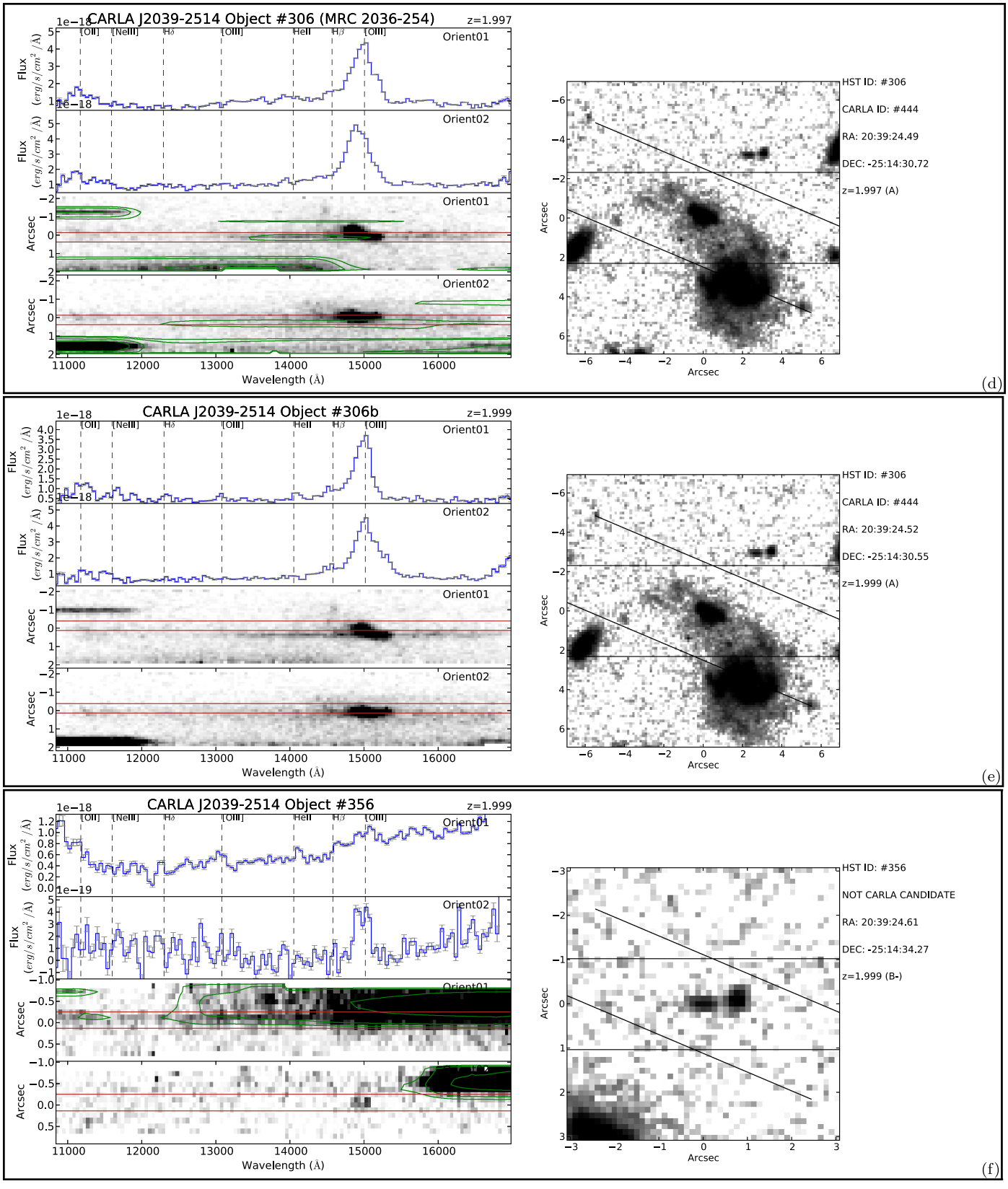

Figure 9. (Continued.)

extracted source in the field, a source outside the field of view, or a shallow emission-line contaminant. However, the emission line at 15000 Å is consistent between both orientations and the source's *Spitzer* color is consistent with [O III] at $z \sim 2$. We measure a redshift of $z = 2.000 \pm 0.007$ from the [O III] emission line. Because of the contamination concerns, the line flux listed in Table 3 is from the second observation. We do

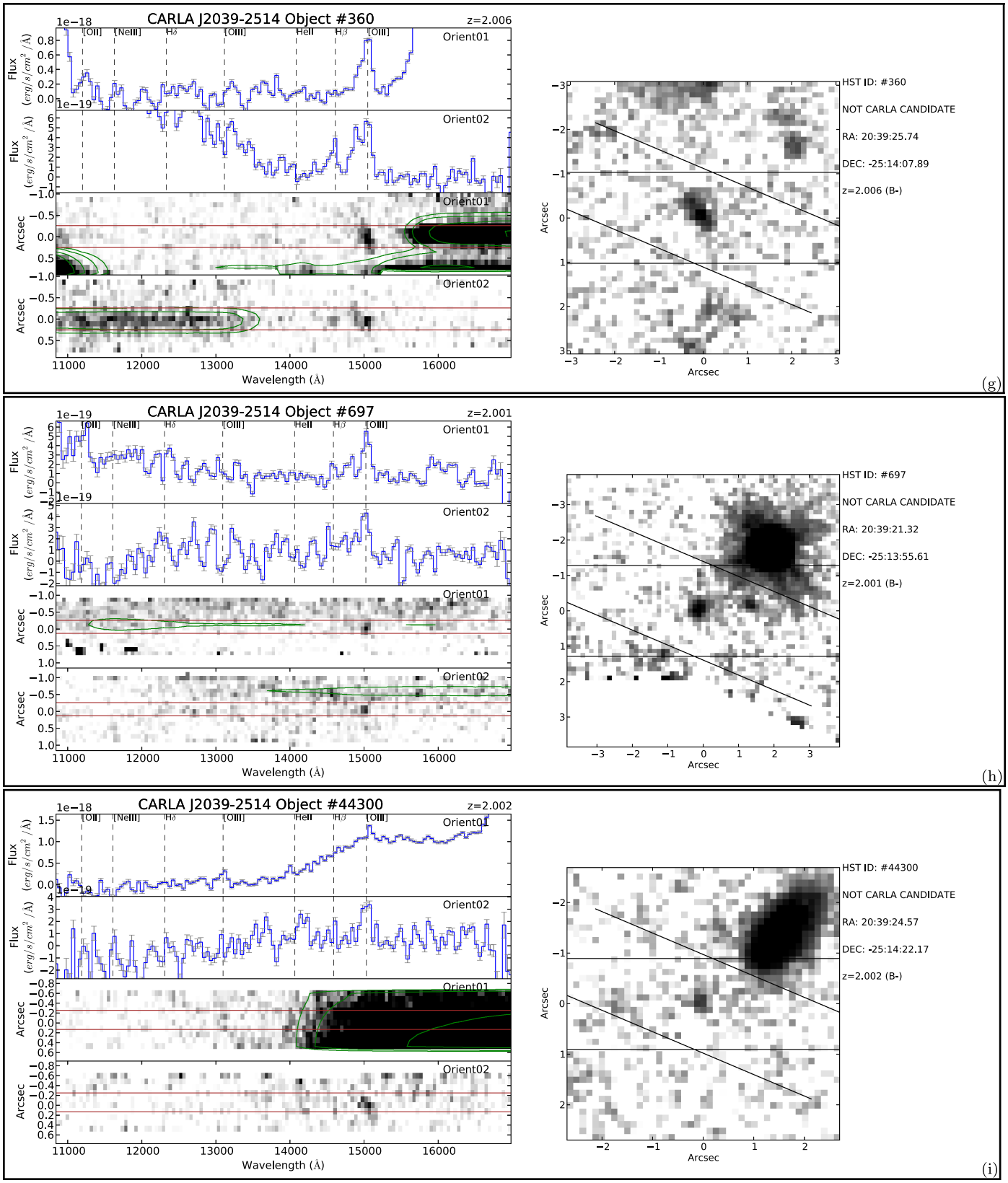

Figure 9. (Continued.)

not detect other lines, and therefore, assign a quality B^+ to this source.

3. *#281:* Another source (#280) is located 1″ from #281. We detect the same emission lines in the #280 spectra as in #281, however, spatially offset above and below the continuum for the former (depending on the observation). Therefore, we associate the emission lines to #281, and we do not exclude #280 as a quiescent companion to

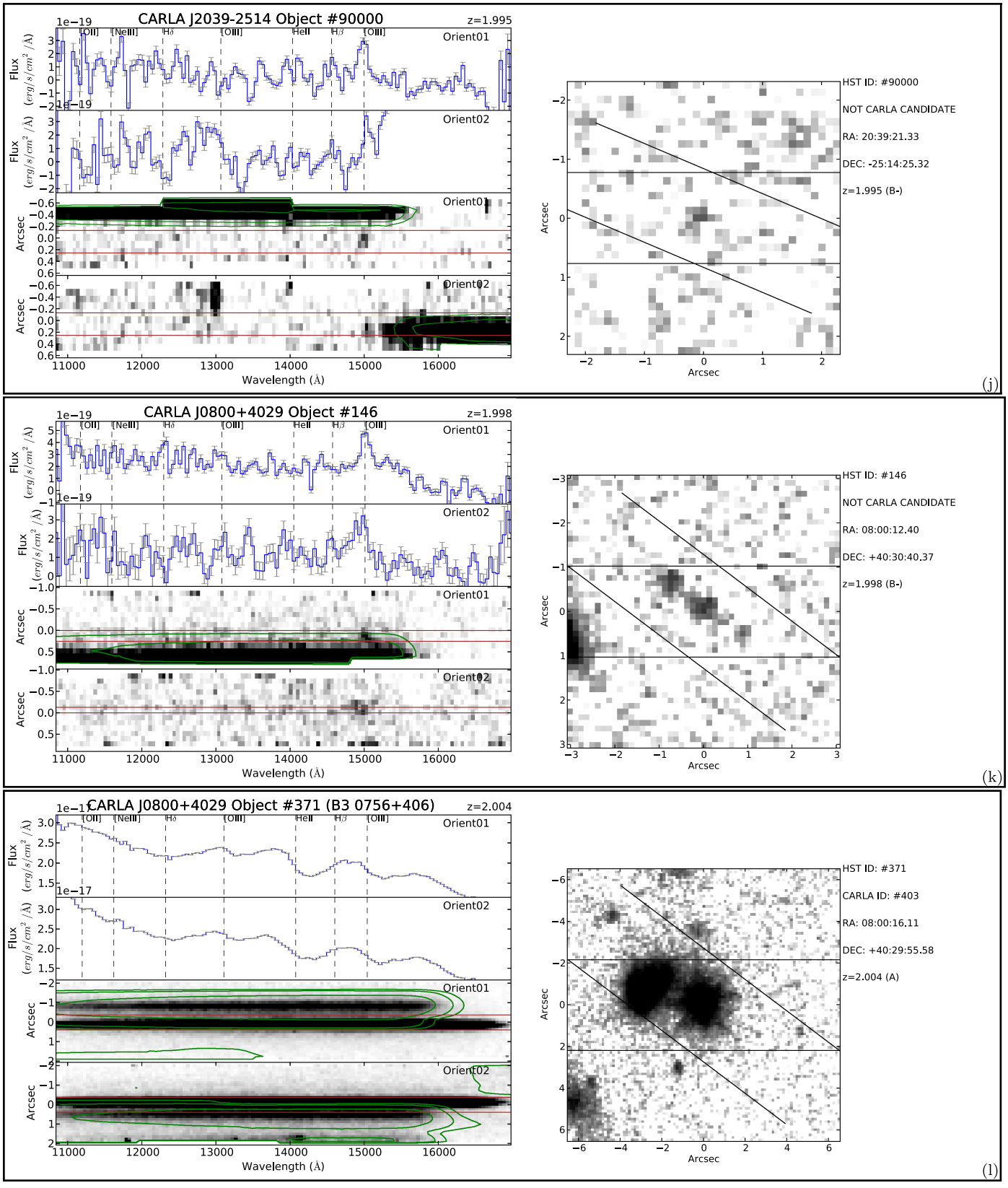

Figure 9. (Continued.)

#281, even though it might be a foreground or background source. The contamination model indicates slight contamination around 15000 Å. The contamination is likely the origin of the broad shape of the line in the second observation, not seen in the first one, and might enhance the true flux of the line, but we still use both orientations to determine the source properties. We measure $z = 2.002 \pm 0.008$ (quality B^-).

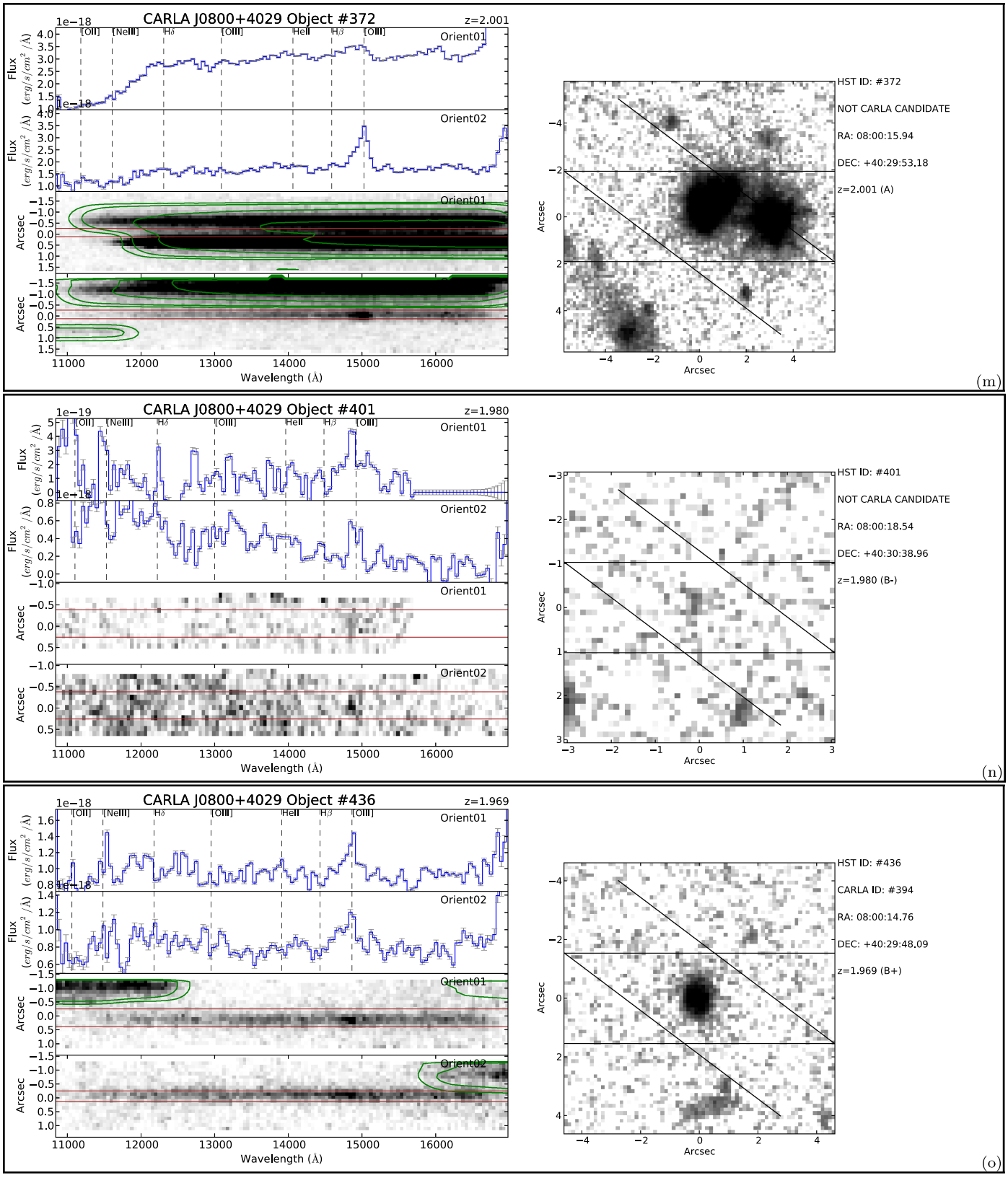

Figure 9. (Continued.)

4. *#356:* Another source (#355) is located 1″ from #356. For similar reasons as for #281, we associate the emission lines to #356, and do not exclude #355 as a quiescent companion to #356. We measure $z = 1.999 \pm 0.005$ (quality B$^-$) from the second observation, as the first one is strongly contaminated by a bright source.
5. *#360:* We detect contamination above 15300 Å in the first observation, and below 14000 Å in the second.

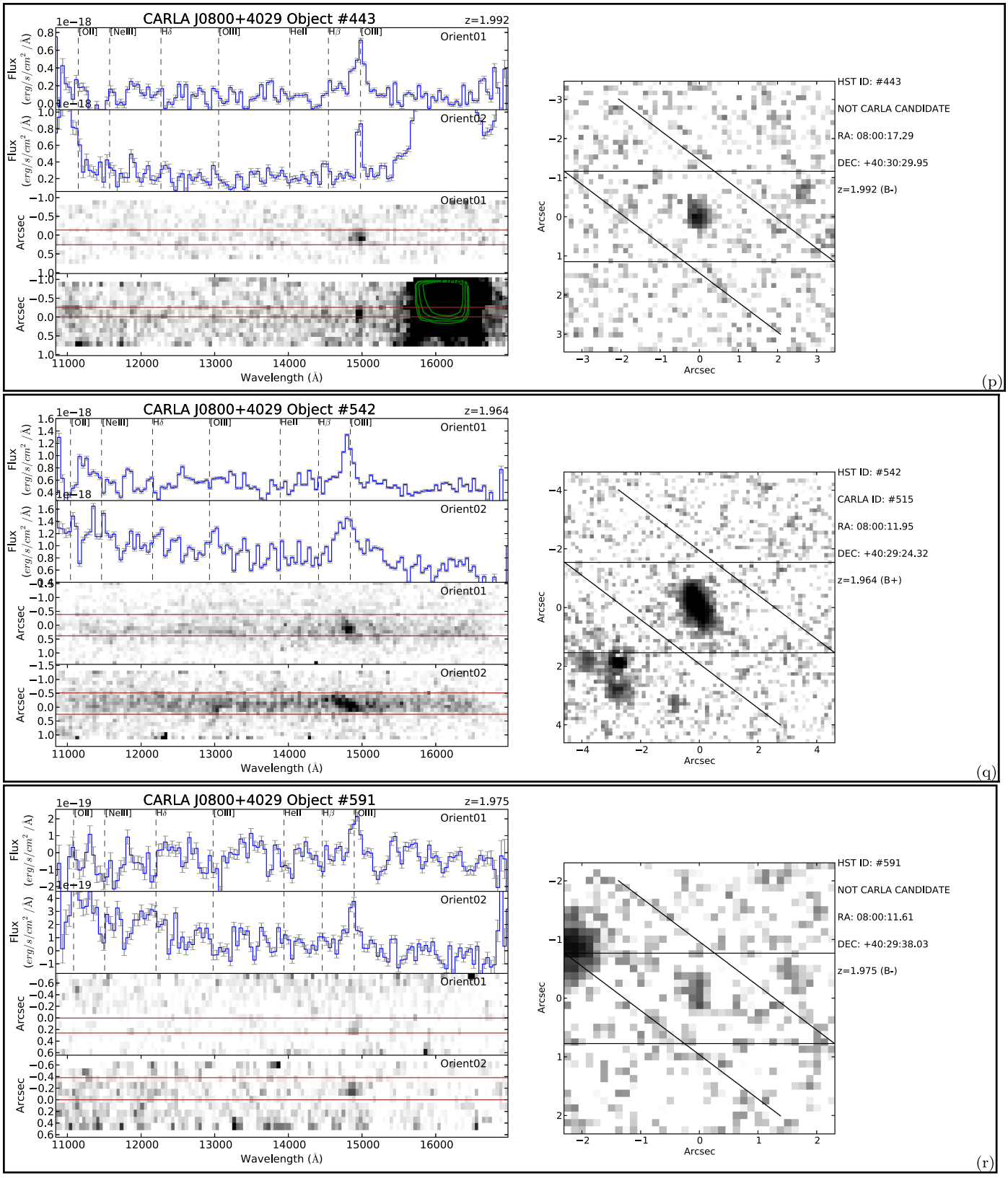

Figure 9. (Continued.)

However, our model does not indicate contamination around the well-detected line at 15050 Å, which we identify as [O III]. We do not identify any other emission lines, and we consider the emission-like feature seen in the second observation at the expected position of Hβ to be due to contamination since it is not present in the first observation. We measure a redshift of $z = 2.006 \pm 0.004$ (quality B$^-$).

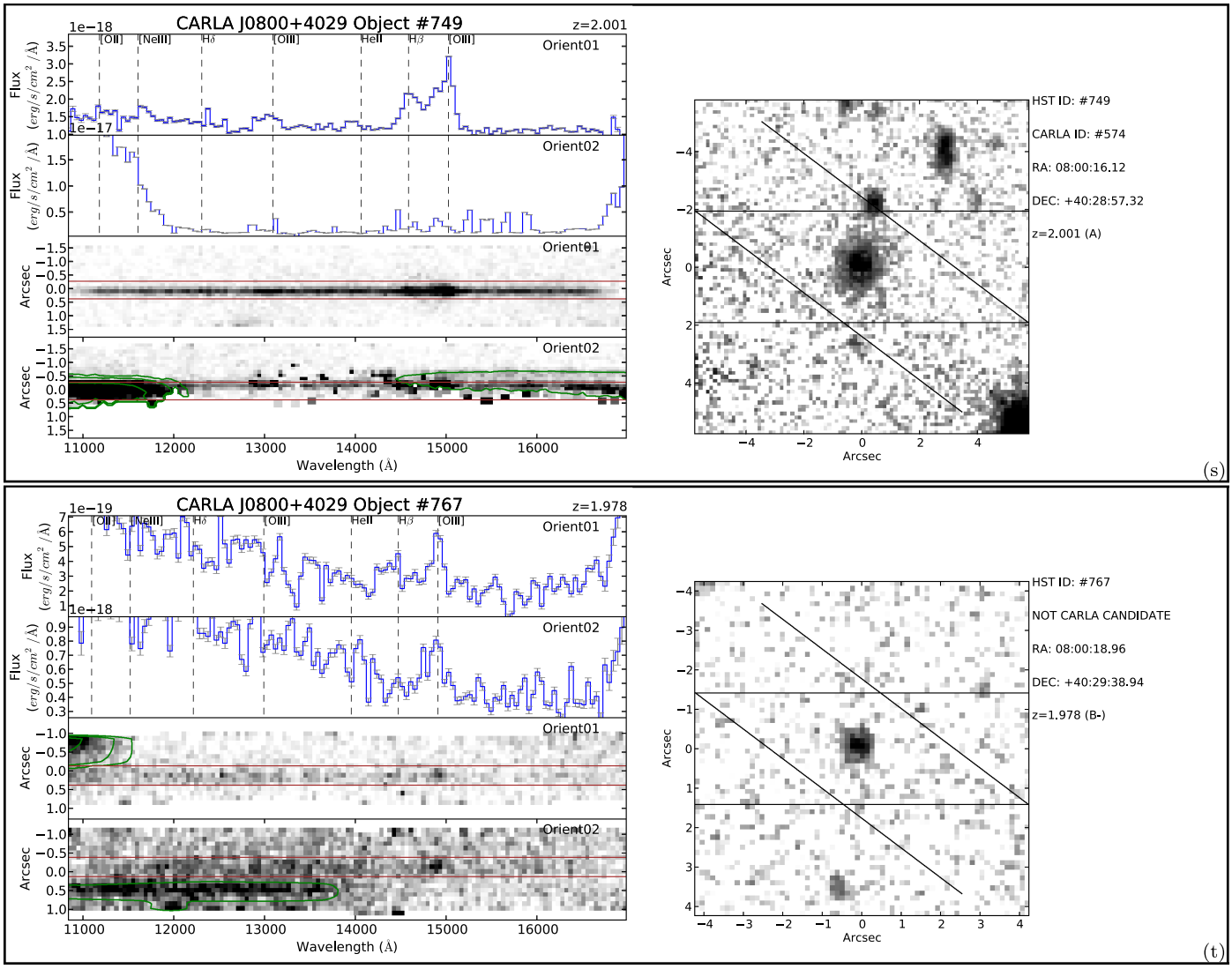

Figure 9. (Continued.)

6. *#697:* The contamination model indicates shallow contamination in the first observation, and spatially offset contamination in the second. We use both observations and determine a quality B$^-$ redshift of $z = 2.001 \pm 0.006$, based on the detection of a single emission line in both orientations.
7. *#44300:* From the second observation, free from contamination, we detect a single emission line, which we associate with [O III] at a redshift of $z = 2.002 \pm 0.005$ (quality B$^-$).
8. *#90000:* The first orientation is free from contamination within our 1D extraction region. The second observation is contaminated longward of the emission line, which affects our spectral modeling. Therefore, we only use the first observation to measure the line parameters in Table 3, providing a quality B$^-$ redshift of $z = 1.995 \pm 0.005$.

D.2. CARLA J0800+4029

1. *#146:* The second observation is free from contaminant. The first observation is contaminated up to 15700 Å, but the contamination is spatially offset by ∼0.″5 from the source. Therefore, we carefully extract the 1D spectrum from the 2D cutout to avoid the contaminant, allowing us to use both observations. We measure a redshift of $z = 1.998 \pm 0.007$ (quality B$^-$).
2. *#401:* The second orientation of this source is visually contaminated below 15000 Å, but we do not have a contamination model associated with this source because it was extracted alone after the main source extraction. We measure a redshift of $z = 1.980 \pm 0.009$ (quality B$^-$).
3. *#436:* This source has a *Spitzer* color consistent with $z > 1.3$. Contamination is detected offset from the source continuum in the 2D cutouts, without overlap. A single line is detected in both observations, providing a quality B$^+$ redshift of $z = 1.969 \pm 0.007$.
4. *#443:* Above 15500 Å, the second observation is contaminated by a zeroth order image of a bright source. We identify an emission line at ∼14980 Å in both observations, but the line is potentially contaminated in the second observation by the mentioned zeroth order. Therefore, we only use the first observation, and measure

a redshift of 1.992 ± 0.004 (quality B^-). The fitting procedure tentatively detects Hβ below our detection limit, and therefore is not taken into account.

5. *#542:* The second observation shows the same emission line as the first observation, but broadened in the dispersion direction (and slightly in the spatial direction). This could be due to the spatial extent of the source, which is more elongated in the dispersion direction of the second observation, or due to an undetected contaminant in the second observation. The mid-infrared *Spitzer* color is consistent with [O III] at $z \sim 2$, but no other emission lines are detected. We use the two observations to measure its redshift and line flux despite the elongated spectral shape of the second observation (note that only using the first observation does not significantly change the results). We measure a redshift of $z = 1.964 \pm 0.007$ (quality B^+).
6. *#591:* Given our contamination model, both observations are free from contaminants. However, we identify in the direct imaging a source located $\sim 2''$ from #591 and likely contaminating part of the spectral 2D cutouts. Therefore, we carefully extract the 1D spectrum from the 2D cutout to avoid potentially contaminated regions, allowing us to use both observations. We measure a redshift of $z = 1.975 \pm 0.007$ (quality B^-).
7. *#767:* This source was detected in our IRAC images and has a *Spitzer* color consistent with [O III] at $z \sim 2$. However, it was not selected as a CARLA candidate because it did not pass our CARLA flux cut. The second observation is contaminated below 14900 Å, with the contamination also somewhat affecting the emission line. The first observation is not contaminated around the emission line at 14910 Å, but is likely contaminated at shorter wavelengths. Using the first observation, we determine a redshift of $z = 1.978 \pm 0.004$, of quality B^+. The observed feature at the expected location of Hβ is likely due to contamination, just at our flux detection limit.

REFERENCES

Abazajian, K., Adelman-McCarthy, J. K., Agüeros, M. A., et al. 2004, AJ, 128, 502
Alberts, S., Pope, A., Brodwin, M., et al. 2014, MNRAS, 437, 437
Alberts, S., Pope, A., Brodwin, M., et al. 2016, arXiv:1604.03564
Andreon, S. 2012, A&A, 548, A83
Bayliss, M. B., Ashby, M. L. N., Ruel, J., et al. 2014, ApJ, 794, 12
Bertin, E., & Arnouts, S. 1996, A&AS, 117, 393
Bleem, L. E., Stalder, B., de Haan, T., et al. 2015, ApJS, 216, 27
Brammer, G. B., van Dokkum, P. G., Franx, M., et al. 2012, ApJS, 200, 13
Brodwin, M., Gonzalez, A. H., Stanford, S. A., et al. 2012, ApJ, 753, 162
Brodwin, M., McDonald, M., Gonzalez, A. H., et al. 2016, ApJ, 817, 122
Brodwin, M., Stanford, S. A., Gonzalez, A. H., et al. 2013, ApJ, 779, 138
Bruzual, G., & Charlot, S. 2003, MNRAS, 344, 1000
Calzetti, D., Armus, L., Bohlin, R. C., et al. 2000, ApJ, 533, 682
Cardelli, J. A., Clayton, G. C., & Mathis, J. S. 1989, ApJ, 345, 245
Carilli, C. L., Röttgering, H. J. A., van Ojik, R., et al. 1997, ApJS, 109, 1
Chabrier, G. 2003, PASP, 115, 763
Chiaberge, M., Gilli, R., Lotz, J. M., & Norman, C. 2015, ApJ, 806, 147
Churazov, E., Vikhlinin, A., & Sunyaev, R. 2015, MNRAS, 450, 1984
Cooke, E. A., Hatch, N. A., Rettura, A., et al. 2015, MNRAS, 452, 2318
Cooke, E. A., Hatch, N. A., Stern, D., et al. 2016, ApJ, 816, 83
Croom, S. M., Smith, R. J., Boyle, B. J., et al. 2004, MNRAS, 349, 1397
De Breuck, C., Seymour, N., Stern, D., et al. 2010, ApJ, 725, 36
Dressel, L. 2014, Wide Field Camera 3 Instrument Handbook, Version 6.0 (Baltimore: STScI)
Drouart, G., De Breuck, C., Vernet, J., et al. 2012, A&A, 548, A45
Eisenhardt, P. R., De Propris, R., Gonzalez, A. H., et al. 2007, ApJS, 169, 225
Eisenhardt, P. R. M., Brodwin, M., Gonzalez, A. H., et al. 2008, ApJ, 684, 905
Ficarra, A., Grueff, G., & Tomassetti, G. 1985, A&AS, 59, 255
Galametz, A., Stern, D., De Breuck, C., et al. 2012, ApJ, 749, 169
Galametz, A., Stern, D., Pentericci, L., et al. 2013, A&A, 559, A2
Galametz, A., Stern, D., Stanford, S. A., et al. 2010, A&A, 516, A101
Gavazzi, G., Pierini, D., & Boselli, A. 1996, A&A, 312, 397
Gladders, M. D., & Yee, H. K. C. 2000, AJ, 120, 2148
Gobat, R., Daddi, E., Onodera, M., et al. 2011, A&A, 526, A133
Gobat, R., Strazzullo, V., Daddi, E., et al. 2013, ApJ, 776, 9
Gonzalez, A. H., Stanford, S. A., Brodwin, M., et al. 2012, ApJ, 753, 163
Grogin, N. A., Kocevski, D. D., Faber, S. M., et al. 2011, ApJS, 197, 35
Hatch, N. A., De Breuck, C., Galametz, A., et al. 2011, MNRAS, 410, 1537
Hatch, N. A., Wylezalek, D., Kurk, J. D., et al. 2014, MNRAS, 445, 280
Hayashi, M., Kodama, T., Koyama, Y., et al. 2010, MNRAS, 402, 1980
Hewett, P. C., & Wild, V. 2010, MNRAS, 405, 2302
Juneau, S., Bournaud, F., Charlot, S., et al. 2014, ApJ, 788, 88
Kapahi, V. K., Athreya, R. M., van Breugel, W., McCarthy, P. J., & Subrahmanya, C. R. 1998, ApJS, 118, 275
Kennicutt, R. C., Jr. 1983, ApJ, 272, 54
Kewley, L. J., Geller, M. J., & Jansen, R. A. 2004, AJ, 127, 2002
Kravtsov, A., Vikhlinin, A., & Meshscheryakov, A. 2014, arXiv:1401.7329
Kümmel, M., Walsh, J., Kuntschner, H., & Bushouse, H. 2011, aXe User Manual version 2.3 (Baltimore: STScI)
Kümmel, M., Walsh, J. R., Pirzkal, N., Kuntschner, H., & Pasquali, A. 2009, PASP, 121, 59
Labbé, I., Huang, J., Franx, M., et al. 2005, ApJL, 624, L81
Large, M. I., Mills, B. Y., Little, A. G., Crawford, D. F., & Sutton, J. M. 1981, MNRAS, 194, 693
Licitra, R., Mei, S., Raichoor, A., Erben, T., & Hildebrandt, H. 2016, MNRAS, 455, 3020
Lidman, C., Rosati, P., Tanaka, M., et al. 2008, A&A, 489, 981
Mancone, C. L., & Gonzalez, A. H. 2012, PASP, 124, 606
Mancone, C. L., Gonzalez, A. H., Brodwin, M., et al. 2010, ApJ, 720, 284
Mandelbaum, R., Li, C., Kauffmann, G., & White, S. D. M. 2009, MNRAS, 393, 377
Mantz, A. B., Abdulla, Z., Carlstrom, J. E., et al. 2014, ApJ, 794, 157
Martini, P., Miller, E. D., Brodwin, M., et al. 2013, ApJ, 768, 1
Massey, P., & Gronwall, C. 1990, ApJ, 358, 344
Matthews, T. A., Morgan, W. W., & Schmidt, M. 1964, ApJ, 140, 35
McCarthy, P. J., Kapahi, V. K., van Breugel, W., et al. 1996, ApJS, 107, 19
Mehta, V., Scarlata, C., Colbert, J. W., et al. 2015, arXiv:1505.07843
Mei, S., Holden, B. P., Blakeslee, J. P., et al. 2009, ApJ, 690, 42
Mei, S., Scarlata, C., Pentericci, L., et al. 2015, ApJ, 804, 117
Miley, G., & De Breuck, C. 2008, A&ARv, 15, 67
Mo, W., Gonzalez, A., Jee, M. J., et al. 2016, ApJL, 818, L25
Momcheva, I. G., Brammer, G. B., van Dokkum, P. G., et al. 2015, arXiv:1510.02106
Muzzin, A., Wilson, G., Demarco, R., et al. 2013, ApJ, 767, 39
Newman, A. B., Ellis, R. S., Andreon, S., et al. 2014, ApJ, 788, 51
Orsi, Á. A., Fanidakis, N., Lacey, C. G., & Baugh, C. M. 2016, MNRAS, 456, 3827
Osterbrock, D. E. (ed.) 1989, Astrophysics of Gaseous Nebulae and Active Galactic Nuclei (Mill Valley, CA: Univ. Science Books)
Overzier, R. A., Harris, D. E., Carilli, C. L., et al. 2005, A&A, 433, 87
Papovich, C. 2008, ApJ, 676, 206
Papovich, C., Momcheva, I., Willmer, C. N. A., et al. 2010, ApJ, 716, 1503
Planck Collaboration XXXIX 2015, arXiv:1508.04171
Rajan, A., et al. 2010, WFC3 Data Handbook, Version 2.1, (Baltimore: STScI)
Rettura, A., Martinez-Manso, J., Stern, D., et al. 2014, ApJ, 797, 109
Rodighiero, G., Daddi, E., Baronchelli, I., et al. 2011, ApJL, 739, L4
Rosati, P., Della Ceca, R., Norman, C., & Giacconi, R. 1998, ApJL, 492, L21
Rykoff, E. S., Rozo, E., Busha, M. T., et al. 2014, ApJ, 785, 104
Salpeter, E. E. 1955, ApJ, 121, 161
Santos, J. S., Fassbender, R., Nastasi, A., et al. 2011, A&A, 531, L15
Schechter, P. 1976, ApJ, 203, 297
Schneider, D. P., Richards, G. T., Hall, P. B., et al. 2010, AJ, 139, 2360
Scoville, N., Aussel, H., Brusa, M., et al. 2007, ApJS, 172, 1
Seymour, N., Stern, D., De Breuck, C., et al. 2007, ApJS, 171, 353
Skelton, R. E., Whitaker, K. E., Momcheva, I. G., et al. 2014, ApJS, 214, 24
Smail, I., Geach, J. E., Swinbank, A. M., et al. 2014, ApJ, 782, 19
Snyder, G. F., Brodwin, M., Mancone, C. M., et al. 2012, ApJ, 756, 114

Spitler, L. R., Labbé, I., Glazebrook, K., et al. 2012, ApJL, 748, L21
Stanford, S. A., Brodwin, M., Gonzalez, A. H., et al. 2012, ApJ, 753, 164
Stern, D., Eisenhardt, P., Gorjian, V., et al. 2005, ApJ, 631, 163
Stern, D., Holden, B., Stanford, S. A., & Spinrad, H. 2003, AJ, 125, 2759
Strazzullo, V., Gobat, R., Daddi, E., et al. 2013, ApJ, 772, 118
Tanaka, M., Finoguenov, A., & Ueda, Y. 2010, ApJL, 716, L152
Tozzi, P., Santos, J. S., Jee, M. J., et al. 2015, ApJ, 799, 93
Tran, K.-V. H., Papovich, C., Saintonge, A., et al. 2010, ApJL, 719, L126
Vanderlinde, K., Crawford, T. M., de Haan, T., et al. 2010, ApJ, 722, 1180
Venemans, B. P., Röttgering, H. J. A., Miley, G. K., et al. 2007, A&A, 461, 823
Vikhlinin, A., Burenin, R. A., Ebeling, H., et al. 2009, ApJ, 692, 1033
Webb, T. M. A., Muzzin, A., Noble, A., et al. 2015, ApJ, 814, 96
Whitaker, K. E., Labbé, I., van Dokkm, P. G., et al. 2011, ApJ, 735, 86
Williams, R. J., Quadri, R. F., Franx, M., van Dokkum, P., & Labbé, I. 2009, ApJ, 691, 1879
Wuyts, S., Labbé, I., Franx, M., et al. 2007, ApJ, 655, 51
Wylezalek, D., Galametz, A., Stern, D., et al. 2013, ApJ, 769, 7
Wylezalek, D., Vernet, J., De Breuck, C., et al. 2014, ApJ, 786, 17
Yuan, T., Nanayakkara, T., Kacprzak, G. G., et al. 2014, ApJL, 795, L20
Zeimann, G. R., Stanford, S. A., Brodwin, M., et al. 2012, ApJ, 756, 115
Zeimann, G. R., Stanford, S. A., Brodwin, M., et al. 2013, ApJ, 779, 137